Available online at www.sciencedirect.com
SCIENCE DIRECT®
Journal of Computational Physics 215 (2006) 172–196
JOURNAL OF COMPUTATIONAL PHYSICS
www.elsevier.com/locate/jcp

A numerical method for simulations of rigid fiber suspensions

Anna-Karin Tornberg [a,*], Katarina Gustavsson [b]

[a] Courant Institute of Mathematical Science, New York University, 251 Mercer Street, New York, NY 10012-1185, United States
[b] Department of Numerical Analysis and Computer Science, KTH, Sweden

Received 10 May 2005; accepted 25 October 2005
Available online 19 December 2005

Abstract

In this paper, we present a numerical method designed to simulate the challenging problem of the dynamics of slender fibers immersed in an incompressible fluid. Specifically, we consider microscopic, rigid fibers, that sediment due to gravity. Such fibers make up the micro-structure of many suspensions for which the macroscopic dynamics are not well understood.

Our numerical algorithm is based on a non-local slender body approximation that yields a system of coupled integral equations, relating the forces exerted on the fibers to their velocities, which takes into account the hydrodynamic interactions of the fluid and the fibers. The system is closed by imposing the constraints of rigid body motions.

The fact that the fibers are straight have been further exploited in the design of the numerical method, expanding the force on Legendre polynomials to take advantage of the specific mathematical structure of a finite-part integral operator, as well as introducing analytical quadrature in a manner possible only for straight fibers.

We have carefully treated issues of accuracy, and present convergence results for all numerical parameters before we finally discuss the results from simulations including a larger number of fibers.

1. Introduction

The ability to accurately predict the physical behavior of a particle-fluid suspension is of great importance since these kinds of materials occur in a large variety of applications, such as manufacturing processes in the paper and pulp industries, clarification of waste-water and medical applications.

In general, the number of particles in such a suspension is extremely large, and it would be desirable to have an accurate mathematical model describing the macroscopic behavior of the system. Indeed, there exist macroscopic models that are based on an averaged description of the suspension. One major difficulty with such a model is however that the averaging process involved leads to unspecified terms. To close the model, constitutive relations for physical parameters such as effective viscosity and permeability are needed. In many cases, these relations depend on the microstructure of the material and are very hard to determine from an experimental point of view since in experiments it can be difficult to isolate one or a few particles and understand their individual dynamics.

* Corresponding author. Tel.: +1 212 998 3299; fax: +1 212 995 4121.
E-mail address: tornberg@cims.nyu.edu (A.-K. Tornberg).

0021-9991/$ - see front matter © 2005 Elsevier Inc. All rights reserved.
doi:10.1016/j.jcp.2005.10.028

In this paper, we are concerned with numerical simulations on the microscale of a suspension with rigid and slender fibers in a viscous fluid. It is well known that the shape of the particles have a large influence on the macroscopic properties of the suspensions and when the suspended particles are slender their orientations strongly affect the rheological properties of the flow.

Numerical simulations performed on the microscale offer the ability to obtain detailed information regarding the microstructure, including the interactions of individual fibers, and the influence on averaged quantities can be studied. To be able to compute averaged quantities that are representative for the macroscopic behavior of the suspension, a relatively large number of particles is likely needed. Hence, the main challenge in the development of a numerical method is to be able to include many particles in the simulation, at a reasonable cost, while maintaining accuracy.

A full discretization of the 3D flow with many slender fibers would be very costly, and approximate methods have to be developed. In this work, we present an accurate numerical method, based on a non-local slender body formulation, for simulating fiber dynamics. We consider slender and microscopic, but non-Brownian, rigid fibers sedimenting due to gravity in a fluid at very low Reynolds numbers, i.e., Stokes flow. This method has been developed drawing from the experience obtained from developing the formulation and a numerical method for interacting flexible fibers in a three-dimensional flow, first presented in [25]. It is certainly possible to simulate the rigid fiber problem by introducing a large bending rigidity for the flexible fibers, but a method specially designed for the rigid fiber case, making use of the simplifications that is offers, will be much more efficient.

The key points in the development of our problem formulation are that for Stokes flow, boundary integral methods can be employed to reduce the three-dimensional dynamics to the dynamics of the two-dimensional fiber surfaces [23], and by using slender body asymptotics [11,17,18], this can be further reduced to the dynamics of the one-dimensional fiber center-lines. The resulting integral equations capture the non-local interaction of the fiber with itself, as well as with any other structures within the fluid, such as other fibers. In doing this we have reduced a full 3D problem to a system of 1D integral equations.

In comparison to the case of flexible fibers, the formulation in the rigid fiber case is simplified by the fact that the fibers can only undergo rigid body motion. Also, an integral operator in the equation is cast in such a form that we are able to use a diagonalization result by Götz [11], thereby avoiding direct evaluation of a finite-part integral that occurs in the formulation.

Our formulation is related to that used by Butler and Shaqfeh [6] in their simulations of the sedimentation of rigid fibers. Both formulations are based on slender-body theory, but we have used a more accurate formulation (of higher order in a slenderness parameter ε) as derived in [11,17,18]. Their formulation is what for a single fiber is called a local drag model, that is the lowest order approximation found in [2]. A local drag model does not take into account the influence of the fiber on the flow, i.e., the fact that one part of the fiber affects the rest of the fiber through induced fluid motion. Butler and Shaqfeh do however include far-field interaction terms to account for the interaction of different fibers. Also here, we have included a modification to these interaction terms to allow for higher accuracy [11]. A lower order slender body formulation was also used by Fan et al. [9], in their simulations of rigid fiber suspensions.

The sedimentation of spherical particles is a problem that has been studied extensively, and a number of different approaches to formulate mathematical models as well as numerical methods have been proposed, see e.g. [1,5,10,20,21]. The results are much more limited for fiber suspensions, in which case the dynamics are quite different, as they strongly depend on the orientation distribution of the fibers.

Butler and Shaqfeh [6] present an extensive study of the sedimentation of fiber suspensions based on numerical computations. The results from the simulations are carefully compared to experimental data and some of the results closely agree. In the paper by Fan et al. [9] a numerical study of fibers in a shear flow is presented. The results are used to compute macroscopic properties of the suspension such as the viscosity. Computer simulations of rod-like particles in a shear flow similar to [9] were earlier presented by Yamane et al. [26]. However in [26], the long range interaction terms are neglected and only short-range hydrodynamic interaction is considered. In related work, Kuusela et al. [19] perform dynamical simulations of prolate spheroids at a low but non-zero Reynolds number with the fluid motion described by the Navier–Stokes equations.

The primary goal of this paper is to present an accurate numerical method developed for the simulation of rigid fiber suspensions, and issues related to the accuracy of the method are carefully examined and convergence

results are presented. We also present results from some larger simulations in the last section, where we have performed simulations to study a few characteristics of the fiber suspension such as mean sedimentation velocity and the orientation of the fibers during the dynamic process. Results from our simulations show, in agreement with what has been reported in e.g. [6,14], that the fibers, starting from a homogeneous distribution, become inhomogeneous and anisotropic and form clusters with fibers entering and leaving the clusters as the simulation proceeds. Many of the fibers align in the direction of gravity and the mean sedimentation velocity do exceed the velocity of a single fiber. Given the wealth of this problem, we look forward to presenting more extensive results and analysis of the results in a forthcoming paper.

The outline of the paper is as follows. In Section 2, we introduce the non-local slender body theory and its derivation. In Section 3, we give the specific equations for the evolution of the rigid fibers. We give the expansion of the force on each fiber in terms of Legendre polynomials, and derive the linear system of equations that determines the coefficients in these expansions, and the evolution equations that can be applied once the forces are known. We also introduce the modifications to these equations necessary to impose periodic boundary conditions. Section 4 is devoted to the numerical method based on this formulation and issues like time stepping, quadrature and solution of the linear system of equations are discussed. We present convergence results and discuss the accuracy of the numerical method in Section 5. Finally, in Section 6, we present results from some larger simulations, including up to 100 fibers, and study quantities such as average sedimentation velocity and fiber orientation.

2. The non-local slender body theory

In this section, we will discuss the non-local slender body theory applied to slender fibers immersed in a fluid.

2.1. Fundamental solutions to the Stokes equations

The flows we are considering are at very low Reynolds numbers, so it is appropriate to consider the Stokes equations. Denote the velocity field by $\mathbf{u}(\mathbf{x})$, the pressure by $p(\mathbf{x})$, and let $\mathbf{f}(\mathbf{x})$ be a force acting on the fluid, where $\mathbf{x} = (x, y, z) \in \mathbb{R}^3$. The Stokes equations read

$$\nabla p - \mu \Delta \mathbf{u} = \mathbf{f} \quad \text{in } \Omega,$$
$$\nabla \cdot \mathbf{u} = 0 \quad \text{in } \Omega,$$

where μ is the viscosity of the fluid.

Now, assume that there are fibers in the flow. Let Γ denote the union of all fiber surfaces and $\mathbf{u}_\Gamma$ the corresponding surface velocity. We impose a no-slip condition on each fiber and require that far away $\mathbf{u}(\mathbf{x})$ is equal to a background velocity $\mathbf{U}_0(\mathbf{x})$, also a solution to the Stokes equations. Hence,

$$\mathbf{u} = \mathbf{u}_\Gamma \quad \text{on } \Gamma, \qquad \mathbf{u} \to \mathbf{U}_0 \quad \text{for } \|\mathbf{x}\| \to \infty.$$

A boundary integral formulation of this problem will include so-called fundamental solutions to the Stokes equations. One such fundamental solution is the Stokeslet. If $\mathbf{f} = \delta(\mathbf{x} - \mathbf{x}_0)\mathbf{e}_i$, with $\mathbf{e}_i$ the unit vector in direction i, then $\mathbf{u}(\mathbf{x}) = \mathbf{S}(\mathbf{x} - \mathbf{x}_0)\mathbf{e}_i$ is a solution to the Stokes equations, with the Stokeslet tensor given by

$$\mathbf{S}(\mathbf{R}) = \frac{1}{8\pi\mu} \frac{\mathbf{I} + \hat{\mathbf{R}}\hat{\mathbf{R}}}{|\mathbf{R}|},$$

where $\mathbf{I}$ is the identity tensor, and $\hat{\mathbf{R}} = \mathbf{R}/|\mathbf{R}|$ a unit vector.

Higher order fundamental solutions can be constructed by differentiation of the Stokeslet. The so-called doublet is defined as

$$\mathbf{D}(\mathbf{R}) = \frac{1}{2}\Delta \mathbf{S}(\mathbf{R}) = \frac{1}{8\pi\mu} \frac{\mathbf{I} - 3\hat{\mathbf{R}}\hat{\mathbf{R}}}{|\mathbf{R}|^3}.$$

2.2. Derivation procedure

A boundary integral formulation for the problem at hand results in integral equations on the surfaces of the fibers [23]. For slender fibers, such a formulation would be very expensive to solve numerically. With a non-local slender body approximation, the integral equations are reduced to the fiber center-lines.

Consider a *slender* fiber; that is $\varepsilon = a/2L \ll 1$, where a is the fiber radius, and $2L$ is its length. We will refer to ε as the slenderness parameter. A non-local slender body approximation can be derived by placing fundamental solutions (Stokeslets and doublets) on the fiber center-line, then applying the technique of matched asymptotics to derive the approximate equation. This step is rather complicated since it requires an inner as well as an outer expansion, and then a reformulation of the outer expansion in terms of the inner variables, so that a matching can be made. The formulation is closed by enforcing a no-slip condition on the fiber surface, assuming the velocity to be a function of arclength only, i.e., that there is no angular variation in fiber velocity.

In this derivation, higher order terms in ε have been neglected, and the accuracy of the final equation for the velocity of the fiber center-line is of order $O(\varepsilon^2 \log \varepsilon)$. This accuracy holds also for a fiber with free ends, if the ends are tapered, see the work by Johnson [17]. For details on the derivation, see the work of Keller and Rubinow [18], Johnson [17] and Götz [11].

The derivation yields an integral equation with a modified Stokeslet kernel on the fiber center-line and relates the fiber forces to the velocity of the center-line that includes the non-local interaction of the fiber with itself, as mediated by the surrounding incompressible fluid. Götz [11] gives an integral expression for the fluid velocity $U(\mathbf{x})$ at any point $\mathbf{x}$ outside the fiber, which is accurate to $O(\varepsilon)$ all the way up to the fiber surface. If there are multiple fibers, their contributions simply add due to the superposition principle of Stokes flow.

2.3. The slender body integral equations

Denote the fibers by Γ_{m}, $\mathsf{m} = 1, \ldots, M$. Let the center-line of each fiber be parameterized by arclength $s \in [-L, L]$, where L is the half length of the fiber and let $\mathbf{x}_{\mathsf{m}}(s,t) = (x_{\mathsf{m}}(s,t), y_{\mathsf{m}}(s,t), z_{\mathsf{m}}(s,t))$ be the coordinates of the fiber center-line. At this point, we have not yet assumed that the fibers are straight.

A non-local slender body approximation [11,17] for the velocity of the center-line for fiber m is given by

$$8\pi\mu\left(\frac{\partial \mathbf{x}_{\mathsf{m}}(s,t)}{\partial t} - \mathbf{U}_0(\mathbf{x}_{\mathsf{m}}(s,t),t)\right) = \Lambda_{\mathsf{m}}[\mathbf{f}_{\mathsf{m}}](s) + \mathbf{K}_{\mathsf{m}}[\mathbf{f}_{\mathsf{m}}](s) + \sum_{\substack{\mathsf{l}=1 \\ \mathsf{l}\neq\mathsf{m}}}^{M} \int_{\Gamma_{\mathsf{l}}} \mathbf{G}(\mathbf{x}_{\mathsf{m}}(s,t) - \mathbf{x}_{\mathsf{l}}(s',t))\mathbf{f}_{\mathsf{l}}(s')\,\mathrm{d}s', \tag{1}$$

where we have assumed that the fluid exerts a force per unit length, $\mathbf{f}_{\mathsf{m}}(s,t)$, upon fiber m. The fluid viscosity is denoted by μ, the sum is over the contributions from all other fibers to the velocity of fiber m, and $\mathbf{U}_0(\mathbf{x},t)$ is the undisturbed background velocity.

The local operator Λ_{m} is given by

$$\Lambda_{\mathsf{m}}[\mathbf{f}](s) = [d(\mathbf{I} + \hat{\mathbf{s}}_{\mathsf{m}}\hat{\mathbf{s}}_{\mathsf{m}}(s)) + 2(\mathbf{I} - \hat{\mathbf{s}}_{\mathsf{m}}\hat{\mathbf{s}}_{\mathsf{m}}(s))]\mathbf{f}(s), \tag{2}$$

with $\hat{\mathbf{s}}_{\mathsf{m}}(s) = \frac{\partial}{\partial s}(\mathbf{x}_{\mathsf{m}}(s))$, the local unit tangent vector. The constant $d = -\log(\varepsilon^2 e)$, $d > 0$, where $\varepsilon = a/2L$ is the slenderness parameter.

The integral operator $\mathbf{K}_{\mathsf{m}}[\mathbf{f}](s)$ is given by

$$\mathbf{K}_{\mathsf{m}}[\mathbf{f}](s) = \int_{-L}^{L} \left(\frac{\mathbf{I} + \hat{\mathbf{R}}_{\mathsf{m}}(s,s')\hat{\mathbf{R}}_{\mathsf{m}}(s,s')}{|\mathbf{R}_{\mathsf{m}}(s,s')|}\mathbf{f}(s') - \frac{\mathbf{I} + \hat{\mathbf{s}}_{\mathsf{m}}(s)\hat{\mathbf{s}}_{\mathsf{m}}(s)}{|s-s'|}\mathbf{f}(s) \right) \mathrm{d}s'. \tag{3}$$

Here, $\mathbf{R}_{\mathsf{m}}(s,s') = \mathbf{x}_{\mathsf{m}}(s) - \mathbf{x}_{\mathsf{m}}(s')$, and $\hat{\mathbf{R}}_{\mathsf{m}} = \mathbf{R}_{\mathsf{m}}/|\mathbf{R}_{\mathsf{m}}|$ is the normalized $\mathbf{R}_{\mathsf{m}}$-vector. The products $\hat{\mathbf{R}}_{\mathsf{m}}\hat{\mathbf{R}}_{\mathsf{m}}$ and $\hat{\mathbf{s}}_{\mathsf{m}}\hat{\mathbf{s}}_{\mathsf{m}}$ are dyadic products, i.e., $(\hat{\mathbf{R}}\hat{\mathbf{R}})_{kl} = \hat{\mathbf{R}}_k\hat{\mathbf{R}}_l$. The operator $\mathbf{K}[\mathbf{f}](s)$ is a so-called finite part integral; each term in the integrand is singular at $s' = s$, and the integral is only well defined when the integrand is kept as the difference of its two terms. Note that the operators Λ_{m} and $\mathbf{K}_{\mathsf{m}}$ both depend on the shape of the fiber, as given by $\mathbf{x}_{\mathsf{m}}(s,t)$.

Finally, $\mathbf{G}(\cdot)$ in the integral defining the velocity disturbance from one fiber to another is given by the sum of a Stokeslet and a doublet,

$$\mathbf{G}(\mathbf{R}) = \frac{\mathbf{I} + \hat{\mathbf{R}}\hat{\mathbf{R}}}{|\mathbf{R}|} + \frac{a^2}{2}\frac{\mathbf{I} - 3\hat{\mathbf{R}}\hat{\mathbf{R}}}{|\mathbf{R}|^3}, \tag{4}$$

with $\hat{\mathbf{R}} = \mathbf{R}/|\mathbf{R}|$ a unit vector.

The equation has been derived assuming that the fiber does not reapproach itself, and that the radius of the fiber is given by $r(s) = \frac{a}{L}\sqrt{L^2 - s^2}$ [17].

The asymptotic accuracy of Eq. (1) in the case of one single fiber in the flow (i.e., no sum included) is $O(\varepsilon^2 \log\varepsilon)$. The velocity $\mathbf{u}(\bar{\mathbf{x}})$ in a field point $\bar{\mathbf{x}}$, due to the presence of fiber l, is given by

$$8\pi\mu(\mathbf{u}(\bar{\mathbf{x}}) - \mathbf{U}_0(\bar{\mathbf{x}})) = \int_{\Gamma_\mathsf{l}} \mathbf{G}(\bar{\mathbf{x}} - \mathbf{x}_\mathsf{l}(s',t))\mathbf{f}_\mathsf{l}(s')\,\mathrm{d}s'. \tag{5}$$

By super position, the contributions from all other fibers to one single fiber simply add, hence yielding Eq. (1). This velocity formula is only accurate to $O(\varepsilon)$ [11]. Formally, the equations for multiple interacting fibers are therefore accurate to $O(\varepsilon)$, even though the most important contribution for each fiber, i.e., the one from the fiber itself, is computed to $O(\varepsilon^2 \log\varepsilon)$.

The local operator Λ_m can also be written as

$$\Lambda_\mathsf{m}[\mathbf{f}](s) = [-\log(\varepsilon^2)(\mathbf{I} + \hat{\mathbf{s}}_\mathsf{m}\hat{\mathbf{s}}_\mathsf{m}(s)) + (\mathbf{I} - 3\hat{\mathbf{s}}_\mathsf{m}\hat{\mathbf{s}}_\mathsf{m}(s))]\mathbf{f}(s).$$

In Eq. (1), the first part of the local operator, written in this form, is that arising in local slender body theory. The remainder, together with the non-local operator $\mathbf{K}_\mathsf{m}[\mathbf{f}]$, includes non-local corrections which capture the global effect on the fluid velocity from the presence of the fiber. Neglecting this contribution, as is done in local theory, means that the effect of the fiber on the fluid is neglected, which is a rather crude approximation, also for a dilute suspension. These terms are of O(1) and is only weakly separated from the leading order term that is logarithmic in ε.

3. Problem formulation

Eq. (1) can be written in a somewhat simpler form when the fibers are straight. Before we do so, let us introduce characteristic length and time scales that will be used to non-dimensionalize the equations.

As the characteristic length, we use the half-length of the fiber, $L_\mathrm{C} = L$. We will consider fibers sedimenting due to buoyancy, so as the characteristic velocity and time, we pick

$$U_\mathrm{C} = \frac{d\Delta\rho g V}{8\pi\mu L}, \quad t_\mathrm{C} = L_\mathrm{C}/U_\mathrm{C} = \frac{8\pi\mu L^2}{d\Delta\rho g V}, \tag{6}$$

where $\Delta\rho$ is the density difference of the fibers and the surrounding fluid, g is the gravitational acceleration, and V is the volume of one fiber. The constant $d = -\log(\varepsilon^2 e)$ was introduced below Eq. (2). These non-dimensional quantities are chosen such that an isolated fiber aligned with gravity will sediment half its length during a non-dimensionalized unit time.

3.1. The slender body equations for rigid straight fibers

We will now work with a non-dimensional form of the equations, such that $s \in [-1, 1]$. In the case of rigid fibers, we can express the coordinates of the centerline of fiber m as $\mathbf{x}_\mathsf{m}(s,t) = \mathbf{x}_\mathsf{m}(t) + s\mathbf{t}_\mathsf{m}(t)$, where $\mathbf{x}_\mathsf{m}$ denotes the center coordinate, and $\mathbf{t}_\mathsf{m}$ the unit tangent vector of the fiber, respectively.

For fiber Γ_m, $\mathsf{m} = 1, \ldots, M$, Eq. (1) becomes

$$d(\dot{\mathbf{x}}_\mathsf{m} + s\dot{\mathbf{t}}_\mathsf{m} - \mathbf{U}_0(\mathbf{x}_\mathsf{m} + s\mathbf{t}_\mathsf{m})) = \Lambda_\mathsf{m}[\mathbf{f}_\mathsf{m}](s) + (I + \mathbf{t}_\mathsf{m}\mathbf{t}_\mathsf{m})\bar{\mathbf{K}}[\mathbf{f}_\mathsf{m}](s) + \sum_{\substack{\mathsf{l}=1 \\ \mathsf{l}\neq\mathsf{m}}}^{M} \int_{-1}^{1} \mathbf{G}(\mathbf{x}_\mathsf{m} + s\mathbf{t}_\mathsf{m} - (\mathbf{x}_\mathsf{l} + s'\mathbf{t}_\mathsf{l}))\mathbf{f}_\mathsf{l}(s')\,\mathrm{d}s', \tag{7}$$

where the dots on $\mathbf{x}_\mathsf{m}$ and $\mathbf{t}_\mathsf{m}$ indicate time derivatives.

The asymptotic parameter $d = -\log(\varepsilon^2 e)$ is again found in the local operator Λ_m, that we now can express as

$$\Lambda_m[\mathbf{f}](s) = [d(\mathbf{I} + \mathbf{t}_m\mathbf{t}_m) + 2(\mathbf{I} - \mathbf{t}_m\mathbf{t}_m)]\mathbf{f}(s), \tag{8}$$

where the unit tangent vector $\mathbf{t}_m$ does not depend on s.

Since the fibers are straight, the integral operator $\mathbf{K}_m$ [$\mathbf{f}$] (s), as defined in Eq. (3), can be written as $(I + \mathbf{t}_m\mathbf{t}_m)\bar{\mathbf{K}}[\mathbf{f}_m](s)$, where $\bar{\mathbf{K}}[\mathbf{f}](s)$ is given by

$$\bar{\mathbf{K}}[\mathbf{f}](s) = \int_{-1}^{1} \frac{\mathbf{f}(s') - \mathbf{f}(s)}{|s' - s|}\, \mathrm{d}s'. \tag{9}$$

In all these expressions, $\mathbf{t}_m\mathbf{t}_m$ is a dyadic product, i.e., $(\mathbf{t}_m\mathbf{t}_m)_{ij} = (\mathbf{t}_m)_i(\mathbf{t}_m)_j$.

Finally, using our non-dimensional formulation, $\mathbf{G}(\cdot)$ in Eq. (4) becomes

$$\mathbf{G}(\mathbf{R}) = \frac{\mathbf{I} + \hat{\mathbf{R}}\hat{\mathbf{R}}}{|\mathbf{R}|} + 2\varepsilon^2 \frac{\mathbf{I} - 3\hat{\mathbf{R}}\hat{\mathbf{R}}}{|\mathbf{R}|^3}. \tag{10}$$

The system of integral equations is closed by the assumption that the fibers are rigid, i.e., they must perform a rigid body rotation, together with the assumption that any external forces applied to the system, such as gravity forces, are known.

3.2. Equations for the forces

In many boundary integral formulations, one knows either the forces acting on the boundaries, or the velocities at the boundaries (such as no-slip conditions on rigid walls). In this case, we know neither the forces acting on the fibers nor the velocity of the fibers. Both will however be determined using the fact that the fibers can only translate and rotate, combined with a knowledge of what external forces that are applied to the system.

In the following, we will let the background velocity $\mathbf{U}_0 = \mathbf{0}$. It can easily be added back in if one so wishes.

Let us introduce the integrated force and the integrated torque for each fiber,

$$\mathbf{F}_m = \int_{-1}^{1} \mathbf{f}_m(s)\, \mathrm{d}s, \quad \mathbf{M}_m = \int_{-1}^{1} s(\mathbf{t}_m \times \mathbf{f}_m(s))\, \mathrm{d}s. \tag{11}$$

These are the external forces and torques applied to the fibers. In the case we are considering here, $\mathbf{F}_m$ will be the gravity force, with a magnitude equal to one due to our non-dimensionalization, and all the external torques will be zero.

By integrating Eq. (7) from -1 to 1, an equation for $\dot{\mathbf{x}}_m$ by itself can be derived. Similarly, an equation for $\dot{\mathbf{t}}_m$ can be obtained. This derivation involves taking a cross product of Eq. (7) with $s\mathbf{t}_m$, then integrating from -1 to 1, and finally taking the cross product with $\mathbf{t}_m$ once more.

Introducing the notation

$$\langle f, g\rangle = \int_{-1}^{1} f(s)g(s)\, \mathrm{d}s \tag{12}$$

and

$$\mathbf{V}_m(s) = \sum_{\substack{l=1 \\ l\neq m}}^{M} \int_{-1}^{1} \mathbf{G}(\mathbf{x}_m + s\mathbf{t}_m - (\mathbf{x}_l + s'\mathbf{t}_l))\mathbf{f}_l(s')\, \mathrm{d}s', \tag{13}$$

we obtain the following equations. First, for $\dot{\mathbf{x}}_m$,

$$d\dot{\mathbf{x}}_m = \frac{1}{2}\Lambda_m[\mathbf{F}_m] + \frac{1}{2}(I + \mathbf{t}_m\mathbf{t}_m)\langle\bar{\mathbf{K}}[\mathbf{f}_m](s), 1\rangle + \frac{1}{2}\langle\mathbf{V}_m(s), 1\rangle, \tag{14}$$

and for $\dot{\mathbf{t}}_{\mathsf{m}}$,

$$d\dot{\mathbf{t}}_{\mathsf{m}} = -\frac{3}{2}(2+d)\mathbf{t}_{\mathsf{m}} \times \mathbf{M}_{\mathsf{m}} + \frac{3}{2}(I - \mathbf{t}_{\mathsf{m}}\mathbf{t}_{\mathsf{m}})\langle \bar{\mathbf{K}}[\mathbf{f}_{\mathsf{m}}](s), s\rangle + \frac{3}{2}(I - \mathbf{t}_{\mathsf{m}}\mathbf{t}_{\mathsf{m}})\langle \mathbf{V}_{\mathsf{m}}, s\rangle. \tag{15}$$

We can now use these two equations to eliminate $\dot{\mathbf{x}}_{\mathsf{m}}$ and $\dot{\mathbf{t}}_{\mathsf{m}}$ from the original Eq. (7). After some algebra, we then obtain a system of equations for $\mathbf{f}_{\mathsf{m}}$, $\mathsf{m} = 1, \ldots, M$, including only computable quantities. The equations read

$$\begin{aligned}\mathbf{f}_{\mathsf{m}}(s) = {} & \frac{1}{2}\mathbf{F}_{\mathsf{m}} + \frac{1}{2(2+d)}\left[I + \frac{2}{d}\mathbf{t}_{\mathsf{m}}\mathbf{t}_{\mathsf{m}}\right]\left(\langle \bar{\mathbf{K}}[\mathbf{f}_{\mathsf{m}}](s), 1\rangle - 2\bar{\mathbf{K}}[\mathbf{f}_{\mathsf{m}}](s)\right) \\ & + \frac{1}{2(2+d)}\left[I - \frac{d-2}{2d}\mathbf{t}_{\mathsf{m}}\mathbf{t}_{\mathsf{m}}\right](\langle \mathbf{V}_{\mathsf{m}}(s), 1\rangle - 2\mathbf{V}_{\mathsf{m}}(s)) \\ & - \frac{3s}{2}(\mathbf{t}_{\mathsf{m}} \times \mathbf{M}_{\mathsf{m}}) + \frac{3s}{2(2+d)}[I - \mathbf{t}_{\mathsf{m}}\mathbf{t}_{\mathsf{m}}](\langle \bar{\mathbf{K}}[\mathbf{f}_{\mathsf{m}}](s), s\rangle + \langle \mathbf{V}_{\mathsf{m}}(s), s\rangle).\end{aligned} \tag{16}$$

To solve these equations, one must make a choice concerning their discretization. We will choose to expand the force as a sum of Legendre polynomials, in order to make use of the result by Götz [11], that the operator $\bar{\mathbf{K}}$ diagonalizes under the Legendre polynomials.

3.3. Computing forces and velocities

Let us denote the Legendre polynomial of degree n by P_n. The Legendre polynomials are orthogonal with respect to the inner product introduced in Eq. (12), and we have that

$$\langle P_n(s), P_k(s)\rangle = \frac{2}{2n+1}\delta_{nk}, \tag{17}$$

where δ_{nk} is the Kronecker delta. The formula for the Legendre polynomials as well as explicit formulas for $P_n(s)$, $n = 1, \ldots, 8$, can be found in Appendix B.

Götz [11,12] has showed that

$$\bar{\mathbf{K}}[P_n(s)\mathbf{e}_i] = \lambda_n P_n(s)\mathbf{e}_i, \quad n \geqslant 0, \tag{18}$$

where $\mathbf{e}_i$ is a unit vector in the ith coordinate direction, and the eigenvalues are given by $\lambda_0 = 0$ and $\lambda_n = 2\sum_{i=1}^{n}(1/i)$, for $n > 0$.

In order to use this result, we expand the force on each fiber as a sum of $N+1$ Legendre polynomials,

$$\mathbf{f}_{\mathsf{m}} = \frac{1}{2}\mathbf{F}_{\mathsf{m}} + \sum_{n=1}^{N}\mathbf{a}_{\mathsf{m}}^{n}P_n(s), \tag{19}$$

where the coefficients $\mathbf{a}_{\mathsf{m}}^{n}$ are vectors with three components. That the constant term must have this form follows from the definition of $\mathbf{F}_{\mathsf{m}}$ in Eq. (11). The number of terms to include in the expansion will be a parameter in the numerical method.

We now use this expansion in Eq. (16), also for $\mathbf{V}_{\mathsf{m}}$, as defined in Eq. (13). We can there after take projections of the resulting equations onto different Legendre polynomials. Using their orthogonality properties, we finally achieve the following system of equations for the force coefficients, for $\mathsf{m} = 1, \ldots, M$:

$$\mathbf{a}_{\mathsf{m}}^{1} + D_1\mathbf{t}_{\mathsf{m}}\mathbf{t}_{\mathsf{m}}\sum_{\substack{\mathsf{l}=1\\ \mathsf{l}\neq\mathsf{m}}}^{M}\sum_{k=1}^{N}\boldsymbol{\Theta}_{\mathsf{lm}}^{k1}\mathbf{a}_{\mathsf{l}}^{k} = \frac{3}{2}(\mathbf{M}_{\mathsf{m}} \times \mathbf{t}_{\mathsf{m}}) - \frac{1}{2}D_1\mathbf{t}_{\mathsf{m}}\mathbf{t}_{\mathsf{m}}\sum_{\substack{\mathsf{l}=1\\ \mathsf{l}\neq\mathsf{m}}}^{M}\boldsymbol{\Theta}_{\mathsf{lm}}^{01}\mathbf{F}_{\mathsf{l}}, \tag{20}$$

$$\mathbf{a}_{\mathsf{m}}^{n} + \gamma_n[I - E_n\mathbf{t}_{\mathsf{m}}\mathbf{t}_{\mathsf{m}}]\sum_{\substack{\mathsf{l}=1\\ \mathsf{l}\neq\mathsf{m}}}^{M}\sum_{k=1}^{N}\boldsymbol{\Theta}_{\mathsf{lm}}^{kn}\mathbf{a}_{\mathsf{l}}^{k} = -\frac{1}{2}\gamma_n[I - E_n\mathbf{t}_{\mathsf{m}}\mathbf{t}_{\mathsf{m}}]\sum_{\substack{\mathsf{l}=1\\ \mathsf{l}\neq\mathsf{m}}}^{M}\boldsymbol{\Theta}_{\mathsf{lm}}^{0n}\mathbf{F}_{\mathsf{l}}, \tag{21}$$

with the second equation for $n = 2, \ldots, N$. Here,

$$\gamma_n = (2n+1)/(2(2+d-\lambda_n)), \quad D_1 = \frac{3}{4}\frac{1}{d-\lambda_1}, \quad E_n = \frac{d-2-\lambda_n}{2(d-\lambda_n)}, \tag{22}$$

where the eigenvalues λ_n are defined below Eq. (18). The 3×3 matrix $\mathbf{\Theta}_{\mathrm{lm}}^{kn}$ is defined as

$$\mathbf{\Theta}_{\mathrm{lm}}^{kn} = \int_{-1}^{1}\left[\int_{-1}^{1}\mathbf{G}(\mathbf{x}_{\mathrm{m}} + s\mathbf{t}_{\mathrm{m}} - (\mathbf{x}_{\mathrm{l}} + s'\mathbf{t}_{\mathrm{l}}))P_k(s')\,\mathrm{d}s'\right]P_n(s)\,\mathrm{d}s, \tag{23}$$

with $\mathbf{G}$ as defined in Eq. (10).

Once the system given by Eqs. (20) and (21) has been solved, the force on each fiber can be computed using Eq. (19).

We now use the force expansion in the equations for $\dot{\mathbf{x}}_{\mathrm{m}}$ and $\dot{\mathbf{t}}_{\mathrm{m}}$ (Eqs. (14) and (15)), again together with the diagonalization result and the orthogonality property of the Legendre polynomials. The translational and rotational velocities for each fiber can then be computed according to

$$\dot{\mathbf{x}}_{\mathrm{m}} = \frac{1}{2d}\Lambda_{\mathrm{m}}\mathbf{F}_{\mathrm{m}} + \frac{1}{d}\sum_{\substack{\mathrm{l}=1\\ \mathrm{l}\neq\mathrm{m}}}^{M}\int_{-1}^{1}\left[\int_{-1}^{1}\mathbf{G}(\mathbf{x}_{\mathrm{m}} + s\mathbf{t}_{\mathrm{m}} - (\mathbf{x}_{\mathrm{l}} + s'\mathbf{t}_{\mathrm{l}}))\mathbf{f}_{\mathrm{l}}(s')\,\mathrm{d}s'\right]\mathrm{d}s, \tag{24}$$

$$\dot{\mathbf{t}}_{\mathrm{m}} = \frac{3}{2}(\mathbf{M}_{\mathrm{m}}\times\mathbf{t}_{\mathrm{m}}) + \frac{1}{d}\sum_{\substack{\mathrm{l}=1\\ \mathrm{l}\neq\mathrm{m}}}^{M}\int_{-1}^{1}\left[\int_{-1}^{1}\mathbf{G}(\mathbf{x}_{\mathrm{m}} + s\mathbf{t}_{\mathrm{m}} - (\mathbf{x}_{\mathrm{l}} + s'\mathbf{t}_{\mathrm{l}}))\mathbf{f}_{\mathrm{l}}(s')\,\mathrm{d}s'\right]s\,\mathrm{d}s. \tag{25}$$

For one single fiber sedimenting due to gravity, with an external force $\mathbf{F}_{\mathrm{g}}$ (gravity), but no external torque applied, we get the simple equations $\dot{\mathbf{x}}_{\mathrm{m}} = \frac{1}{2d}\Lambda_{\mathrm{m}}\mathbf{F}_{\mathrm{m}} = \frac{1}{2d}\Lambda_{\mathrm{m}}\mathbf{F}_g$, and $\dot{\mathbf{t}}_{\mathrm{m}} = 0$. Hence, no matter the orientation of the fiber, it will not rotate, which is a known result for Stokes flow limit [14]. If the fiber is aligned with the direction of gravity, $\mathbf{t}_{\mathrm{m}}\mathbf{t}_{\mathrm{m}}\mathbf{F}_{\mathrm{g}} = \mathbf{F}_{\mathrm{g}}$, and we get

$$\dot{\mathbf{x}}_{\mathrm{m}} = \frac{1}{2d}\Lambda_{\mathrm{m}}\mathbf{F}_g = \frac{1}{2d}[d(\mathbf{I}+\mathbf{t}_{\mathrm{m}}\mathbf{t}_{\mathrm{m}}) + 2(\mathbf{I}-\mathbf{t}_{\mathrm{m}}\mathbf{t}_{\mathrm{m}})]\mathbf{F}_g = \frac{1}{2d}[d(\mathbf{F}_g+\mathbf{F}_g) + 2(\mathbf{F}_g-\mathbf{F}_g)] = \mathbf{F}_g.$$

With $\mathbf{F}_{\mathrm{g}} = (0,0,1)$, the velocity is unity, and the fiber will sediment half its length in unit time. This is how we picked our non-dimensionalization.

3.4. Close approach

As two fibers get within close proximity of each other, it is desirable to include a more accurate treatment of their interactions than what is described by the slender body theory. When the distance between the fibers gets small, the forces between them, called lubrication forces, get very large, since they scale with the inverse distance.

There are analytic formulas, in terms of an expansion in the separation distance, for the lubrication forces that occur as two rods approach each other with a given velocity. Cox [8] derived the leading order term for the normal components of the forces. The leading normal term scale as the inverse of this separation distance, while the leading terms of the two other components scale as the logarithm of this inverse distance. Claeys and Brady [7] derived also the explicit expressions for the logarithmic lower order terms in these expansions.

Yamane et al. [26] used the leading order term in the normal direction as their approximation to the lubrication force when the gap between two fibers is less than a certain value. The equation for the fiber motions of this fiber pair was based on a local drag model, neglecting non-local interactions. For fibers at a larger distance, all interactions were ignored, i.e., also the long range interactions. Fan et al. [9] used the same treatment of lubrication forces as Yamane et al., ignoring all non-local interactions for fibers within a pair of two close fibers, arguing that the local lubrication forces dominate for these fibers. For fibers further apart, they did however include non-local interactions through a slender body formulation.

In the paper by Butler and Shaqfeh [6], the velocities in one time step are taken as the given velocities with which the fibers approach each other, and the lubrication forces are then computed for a pair of fibers based on these velocities, again as given by the leading order term for the normal component [7,8]. In the next time step, these lubrication forces are added as external forces to the system, with opposite signs for the two fibers.

In addition to the formulas used by Yamane et al. and Fan et al. for two non-parallel cylindrical rods, Butler and Shaqfeh also include formulas for the lubrication forces between two parallel ellipsoidal bodies, between a sphere (modeling the end-cap of a fiber) and a cylindrical body, and between two spheres (interaction of two end-caps), switching between the formulas depending on the relative position of the fibers.

For a more accurate treatment, one would however, in addition to having an accurate model for the lubrication forces, need to subtract off the contribution from the slender body equations, or only add higher order corrections.

In our formulation, we have included the dipole in our definition of $\mathbf{G}(\cdot)$ in Eq. (10). Doing so, the error in the velocity formula (5) is $O(\varepsilon)$ as we approach the fiber surface instead of $O(1)$ without it. For our formulation, we can see no gain in adding approximations of the lubrication forces in the manner described above, and will at this point not modify it. We do however intend to return to this issue at a later time, carefully analyzing how this can be done in a consistent manner.

3.5. Periodic boundary conditions

To introduce periodic boundary conditions, we need to include the contribution not only from other fibers in the flow, but also from all periodic images of all fibers.

Now, denote the first part of $\mathbf{G}(\mathbf{R})$ in Eq. (10), the Stokeslet, by $\mathbf{S}(\mathbf{R})$ such that

$$\mathbf{S}(\mathbf{R}) = \frac{\mathbf{I} + \hat{\mathbf{R}}\hat{\mathbf{R}}}{|\mathbf{R}|}. \tag{26}$$

We will only include the periodic contribution from this part of $\mathbf{G}(\mathbf{R})$ since the dipole has a coefficient of ε^2 and also a much more rapid decay than the Stokeslet.

Introduce a periodic box of size $\gamma_x \times \gamma_y \times \gamma_z$. Let

$$\mathbf{p} = p_1\gamma_x\hat{\mathbf{x}} + p_2\gamma_y\hat{\mathbf{y}} + p_3\gamma_z\hat{\mathbf{z}}, \tag{27}$$

where $\hat{\mathbf{x}} = (1,0,0)$, $\hat{\mathbf{y}} = (0,1,0)$, and $\hat{\mathbf{z}} = (0,0,1)$. The sum defining a periodic Stokeslet, or a periodic Green's function for Stokes flow,

$$\sum_{p_1,p_2,p_3 \in Z} \mathbf{S}(\mathbf{R} + \mathbf{p}),$$

where the sum is a triple sum, is however divergent.

To make this sum convergent, and hence the corresponding fluid velocity well defined, we must assume that the gravitational forces acting on all the fibers are balanced by a mean pressure gradient of the fluid. Expressing the Stokes equations in Fourier space, this assumption corresponds to omitting the zero wave number term in the expansion of the periodic Stokeslet.

Unfortunately, a pure Fourier series representation converges slowly, making it unfit for practical computations. One way to speed up these calculations is to use a fast summation method, based on Ewald's original summation formula, as given by Hasimoto [13].

We have however based our method on a different formulation, as given by Pozrikidis [24], based on the work by Beenakker [3]. The sum is decomposed into one sum in real space, that decays in a Gaussian manner, and one sum in Fourier space with an exponential decay.

Let us denote the resulting periodic Stokeslet by $\mathbf{S}_{\mathrm{p}}(\mathbf{R})$. We introduce the decomposition

$$\mathbf{S}_{\mathrm{p}}(\mathbf{R}) = \mathbf{S}(\mathbf{R}) + \tilde{\mathbf{S}}_{\mathrm{p}}(\mathbf{R}), \tag{28}$$

such that the singular behavior as $|\mathbf{R}|$ tends to zero is included in $\mathbf{S}(\mathbf{R})$ (defined in Eq. (26)), and all components of $\tilde{\mathbf{S}}_{\mathrm{p}}(\mathbf{R})$ are smooth.

We have

$$\tilde{\mathbf{S}}_{\mathrm{p}}(\mathbf{R}) = \tilde{\boldsymbol{\Upsilon}}(\mathbf{R}) + \sum_{\substack{p_1,p_2,p_3 \in Z \\ |\mathbf{p}| \neq 0}} \boldsymbol{\Upsilon}(\mathbf{R} + \mathbf{p}) + \frac{1}{\tau} \sum_{\substack{k_1,k_2,k_3 \in Z \\ |\mathbf{k}| \neq 0}} \hat{\boldsymbol{\Phi}}(\mathbf{k}, \mathbf{R}). \tag{29}$$

Here, we have three parts; a center part, a sum in real space and a sum in reciprocal space. The first part is given by

$$\tilde{\Upsilon}(\mathbf{x}) = \frac{\tilde{C}(\xi|\mathbf{x}|)}{|\mathbf{x}|}\mathbf{I} + \frac{\tilde{D}(\xi|\mathbf{x}|)}{|\mathbf{x}|}\hat{\mathbf{x}}\hat{\mathbf{x}},$$

where $\hat{\mathbf{x}} = \mathbf{x}/|\mathbf{x}|$, and

$$\tilde{C}(r) = -\mathrm{erf}(r) + \frac{2}{\sqrt{\pi}}(2r^2 - 3)re^{-r^2}, \quad \tilde{D}(r) = -\mathrm{erf}(r) + \frac{2}{\sqrt{\pi}}(1 - 2r^2)re^{-r^2}, \tag{30}$$

where $\xi > 0$ is a free parameter. The error function is defined as

$$\mathrm{erf}(r) = \frac{2}{\sqrt{\pi}}\int_0^r e^{-t^2}\,dt \tag{31}$$

and the complimentary error function as $\mathrm{erfc}(r) = 1 - \mathrm{erf}(r)$. To define $\tilde{\Upsilon}(\mathbf{R})$ when $\mathbf{R} = \mathbf{0}$, we must use the limits

$$\lim_{|\mathbf{x}|\to 0}\frac{\tilde{C}(\xi|\mathbf{x}|)}{|\mathbf{x}|} = -\frac{8\xi}{\sqrt{\pi}}, \quad \text{and} \quad \lim_{|\mathbf{x}|\to 0}\frac{\tilde{D}(\xi|\mathbf{x}|)}{|\mathbf{x}|} = 0. \tag{32}$$

For the sum in real space, the vector $\mathbf{p}$ is defined in Eq. (27), and

$$\Upsilon(\mathbf{x}) = \frac{C(\xi|\mathbf{x}|)}{|\mathbf{x}|}\mathbf{I} + \frac{D(\xi|\mathbf{x}|)}{|\mathbf{x}|}\hat{\mathbf{x}}\hat{\mathbf{x}}, \tag{33}$$

with

$$C(r) = \mathrm{erfc}(r) + \frac{2}{\sqrt{\pi}}(2r^2 - 3)re^{-r^2}, \quad D(r) = \mathrm{erfc}(r) + \frac{2}{\sqrt{\pi}}(1 - 2r^2)re^{-r^2}. \tag{34}$$

For the sum in reciprocal space, we have $\tau = \gamma_x\gamma_y\gamma_z$, the reciprocal vector

$$\mathbf{k} = k_1(2\pi/\gamma_x)\hat{\mathbf{x}} + k_2(2\pi/\gamma_y)\hat{\mathbf{y}} + k_3(2\pi/\gamma_z)\hat{\mathbf{z}}, \tag{35}$$

and

$$\hat{\Phi}(\mathbf{k}, \mathbf{R}) = \frac{8\pi}{\xi^4}\left(\frac{1}{\omega^4} + \frac{1}{4}\frac{1}{\omega^2} + \frac{1}{8}\right)(\mathbf{I}|\mathbf{k}|^2 - \mathbf{k}\mathbf{k})e^{i\mathbf{k}\cdot\mathbf{R}}e^{-\omega^2/4}, \tag{36}$$

($|\mathbf{k}| \neq 0$) which is exponentially decaying in $\omega = |\mathbf{k}|/\xi$. Both sums in the definition of $\tilde{\mathbf{S}}_p(\mathbf{R})$ have a rapid decay.

Some complimentary details and a discussion of the derivation of the formula for $\tilde{\mathbf{S}}_p(\mathbf{R})$, as given in Eq. (29), can be found in Appendix A. Let us here only emphasize that the final result does not depend on the choice of ξ, this choice only affects the rate of decay of the terms in the real and reciprocal sum, respectively. The computation of $\tilde{\mathbf{S}}_p(\mathbf{R})$, including the choice of ξ, is discussed in Section 4.4.

Finally, we can state the evolution equations in the periodic case. For fiber Γ_m, $m = 1, \ldots, M$, Eq. (7) becomes

$$d(\dot{\mathbf{x}}_m + s\dot{\mathbf{t}}_m - \mathbf{U}_0(\mathbf{x}_m + s\mathbf{t}_m)) = \Lambda_m[\mathbf{f}_m](s) + (I + \mathbf{t}_m\mathbf{t}_m)\bar{\mathbf{K}}[\mathbf{f}_m](s) + \sum_{\substack{l=1\\ l\neq m}}^{M}\int_{-1}^{1}\mathbf{G}(\mathbf{x}_m + s\mathbf{t}_m - (\mathbf{x}_l + s'\mathbf{t}_l))\mathbf{f}_l(s')\,ds'$$
$$+ \sum_{l=1}^{M}\int_{-1}^{1}\tilde{\mathbf{S}}_p(\mathbf{x}_m + s\mathbf{t}_m - (\mathbf{x}_l + s'\mathbf{t}_l))\mathbf{f}_l(s')\,ds', \tag{37}$$

where $\mathbf{S}(\cdot)$ in the decomposition in Eq. (28) is a part of $\mathbf{G}(\cdot)$ as defined in Eq. (10). The final equations that we use in the non-periodic case are Eqs. (20)–(25). For the periodic case, we modify Eqs. (20), (21), such that the sums also include $l = m$, with Θ_{lm}^{kn} replaced by $\tilde{\Theta}_{lm}^{kn}$, where

$$\tilde{\Theta}_{lm}^{kn} = \int_{-1}^{1}\left[\int_{-1}^{1}\mathbf{G}_p^{lm}(\mathbf{x}_m + s\mathbf{t}_m - (\mathbf{x}_l + s'\mathbf{t}_l))P_k(s')\,ds'\right]P_n(s)\,ds, \tag{38}$$

where

$$\mathbf{G}_{\mathrm{p}}^{\mathsf{lm}}(\mathbf{R}) = \begin{cases} \mathbf{G}(\mathbf{R}) + \tilde{\mathbf{S}}_{\mathrm{p}}(\mathbf{R}) & \text{if } \mathsf{l} \neq \mathsf{m}, \\ \tilde{\mathbf{S}}_{\mathrm{p}}(\mathbf{R}) & \text{if } \mathsf{l} = \mathsf{m}, \end{cases} \tag{39}$$

with $\mathbf{G}(\mathbf{R})$ and $\tilde{\mathbf{S}}_{\mathrm{p}}(\mathbf{R})$ as defined in Eqs. (10) and (29), respectively.

The translational and rotational velocities for each fiber can then be computed according to

$$\dot{\mathbf{x}}_{\mathsf{m}} = \frac{1}{2d}\Lambda_{\mathsf{m}}\mathbf{F}_{\mathsf{m}} + \frac{1}{d}\sum_{\mathsf{l}=1}^{M}\int_{-1}^{1}\left[\int_{-1}^{1}\mathbf{G}_{\mathrm{p}}^{\mathsf{lm}}(\mathbf{x}_{\mathsf{m}} + s\mathbf{t}_{\mathsf{m}} - (\mathbf{x}_{\mathsf{l}} + s'\mathbf{t}_{\mathsf{l}}))\mathbf{f}_{\mathsf{l}}(s')\,\mathrm{d}s'\right]\mathrm{d}s, \tag{40}$$

$$\dot{\mathbf{t}}_{\mathsf{m}} = \frac{3}{2}(\mathbf{M}_{\mathsf{m}} \times \mathbf{t}_{\mathsf{m}}) + \frac{1}{d}\sum_{\mathsf{l}=1}^{M}\int_{-1}^{1}\left[\int_{-1}^{1}\mathbf{G}_{\mathrm{p}}^{\mathsf{lm}}(\mathbf{x}_{\mathsf{m}} + s\mathbf{t}_{\mathsf{m}} - (\mathbf{x}_{\mathsf{l}} + s'\mathbf{t}_{\mathsf{l}}))\mathbf{f}_{\mathsf{l}}(s')\,\mathrm{d}s'\right]s\,\mathrm{d}s. \tag{41}$$

4. The numerical method

To define the position and orientation of each fiber, we need only to store the center coordinate $\mathbf{x}_{\mathsf{m}}$ and the orientation (i.e., tangent) vector $\mathbf{t}_{\mathsf{m}}$.

Given the instantaneous positions of all fibers, the coefficients in the force expansion for each fiber can be determined by solving the system of equations as defined in Eqs. (20) and (21). The fact that the forces are determined by the instantaneous positions of all fibers is due to the Stokes flow limit, where there are no effects of inertia. The translational ($\dot{\mathbf{x}}_{\mathsf{m}}$) and rotational ($\dot{\mathbf{t}}_{\mathsf{m}}$) velocities, $m = 1, \ldots, M$, can then be computed using Eqs. (24) and (25).

To formulate the numerical method, there are a few different choices to be made. We have already chosen to expand the forces as a sum of $N+1$ Legendre polynomials, where N will be a parameter of the numerical method. To update the position of the fibers, Eqs. (24) and (25) must be discretized in time. We must also choose how to evaluate the integrals in Eqs. (20), (21) and (24), (25), and how to solve the system of equations for the Legendre coefficients in the expansion of the forces, defined in Eqs. (20) and (21). In the periodic case Eqs. (40) and (41) are used instead of Eqs. (24) and (25).

4.1. Time stepping

An explicit time-stepping scheme can be employed for Eqs. (24) and (25) as well as Eqs. (40) and (41) since there are no terms in the equations that impose a strict stability restriction. We have used a second order multi-step method. Note that these equations are ordinary differential equations, the dependence of s has been integrated away.

Starting at $t = 0$, we choose a time step Δt, and denote $t_i = i\Delta t$ and $\mathbf{x}_{\mathsf{m}}^i$ the numerical approximation of $\mathbf{x}_{\mathsf{m}}(t_i)$. With the schematic notation

$$\dot{\mathbf{x}}_{\mathsf{m}} = \mathbf{g}(t), \tag{42}$$

the discretization is given by

$$\frac{3\mathbf{x}_{\mathsf{m}}^{i+1} - 4\mathbf{x}_{\mathsf{m}}^{i} + \mathbf{x}_{\mathsf{m}}^{i-1}}{2\Delta t} = (2\mathbf{g}^{i} - \mathbf{g}^{i-1}). \tag{43}$$

To initialize this scheme, we need both $\mathbf{x}_{\mathsf{m}}^0$ and $\mathbf{x}_{\mathsf{m}}^1$. In the first time step, $\mathbf{x}_{\mathsf{m}}^1$ is computed with the first order forward Euler method. The same discretization is used for $\dot{\mathbf{t}}_{\mathsf{m}}$ in Eq. (25) or Eq. (41).

4.2. Quadrature

The linear system for the Legendre coefficients in the expansion of the force is defined in Eqs. (20) and (21). To compute the matrix entries and right-hand side for this system, the integral in Eq. (23) has to be evaluated for each fiber pair, for $k = 0, \ldots, N$, $n = 1, \ldots, N$, where N is the highest order Legendre polynomial included in the expansion.

This can accurately be done by employing a standard quadrature rule as long as the distance between two fibers is not very small. However, as the fibers get closer, a large number of quadrature points would be needed to ensure that the integrals are evaluated accurately.

For the inner integral in Eq. (23), with $\mathbf{G}(\cdot)$ as defined in Eq. (10), one can however develop formulas for analytic integration. For any s, let $\bar{\mathbf{x}} = \mathbf{x}_m + s\mathbf{t}_m$ and $\mathbf{R}(s') = \bar{\mathbf{x}} - (\mathbf{x}_l + s'\mathbf{t}_l)$. Introducing $\mathbf{R}_0 = \bar{\mathbf{x}} - \mathbf{x}_l$ such that $\mathbf{R}(s') = \mathbf{R}_0 - s'\mathbf{t}_l$, we can write the inner integral as

$$\int_{-1}^{1} \mathbf{G}(\mathbf{R}(s'))P_k(s')\,\mathrm{d}s' = L_k^{0,1} I + L_k^{0,3}\mathbf{R}_0\mathbf{R}_0 - L_k^{1,3}(\mathbf{t}_l\mathbf{R}_0 + \mathbf{R}_0\mathbf{t}_l) + L_k^{2,3}\mathbf{t}_l\mathbf{t}_l + 2\varepsilon^2(L_k^{0,3} I - 3L_k^{0,5}\mathbf{R}_0\mathbf{R}_0 + 3L_k^{1,5}(\mathbf{t}_l\mathbf{R}_0 + \mathbf{R}_0\mathbf{t}_l) - 3L_k^{2,5}\mathbf{t}_l\mathbf{t}_l),$$

where

$$L_k^{\alpha,\beta} = \int_{-1}^{1} \frac{s^\alpha P_k(s)}{(\sqrt{s^2 + bs + c})^\beta}\,\mathrm{d}s, \tag{44}$$

with $b = -2\mathbf{t}_l \cdot \mathbf{R}_0$, and $c = |\mathbf{R}_0|^2$. Expanding the Legendre polynomials, the nominators will be powers of s, with the highest power $\alpha + k$. These integrals can be evaluated efficiently for $k = 0, \ldots, N$, using recursive formulas. This is further described in Appendix B.

The outer integral is evaluated by splitting the integration interval into N_q sub intervals, using a three point Gauss quadrature rule on each interval (as given in Appendix B). This quadrature rule is sixth order accurate.

We always use the analytic integration for the inner integral when computing $\mathbf{\Theta}_{lm}^{kn}$ (Eq. (23)), not only when the fibers are close. It is faster than evaluating the integrals with a three point Gauss quadrature rule as described above. With $N_q = 8$ integration intervals, i.e., a total of $3 \times N_q = 24$ quadrature points, the cpu time is approximately four times less when analytical integration is used compared to numerical quadrature.

There is some concern regarding the sensitivity of the recursion formulas used for the analytical integration to round off errors. This occurs for Legendre polynomials of high degree (large N) when the fibers are far apart and b and c become large. However, the effects on the numerical results are small since when the distance between two fibers is large $\mathbf{\Theta}_{lm}^{kn}$ will be almost zero for large values of N.

4.3. Linear system of equations

Due to the fiber–fiber interactions, the linear system of equations as defined by Eqs. (20) and (21) is a full system. We are solving for N unknown coefficients in the Legendre expansion for each fiber, where each coefficient is a vector with three components. With M fibers, the number of unknowns is $3MN$.

The linear system can either be solved by a direct solver or an iterative method. Since the assembly of the system requires computation of all the integrals discussed above, this comprises a substantial part of the computational effort.

An iterative method in which the matrix is not stored, but where rather a matrix–vector product is directly computed in each iteration, will therefore have a high cost per iteration, since the integrals must be recomputed. Therefore, such a method is not competitive unless it requires only very few iterations to converge at all times, something that will not be the case.

Hence, we will only compute the integrals once and store the matrix entries. The M diagonal blocks of the matrix are identity matrices of size $3N \times 3N$, but the off-diagonal blocks have no such structure. The matrix is not symmetric. It cannot be guaranteed to be diagonally dominant – the off-diagonal entries get larger as fibers come in close proximity of each other.

Considering these characteristics of the matrix, we solve the system iteratively with the GMRES method.

4.4. Periodicity

In the case of periodic boundary conditions, we need to evaluate $\tilde{\mathbf{S}}_p(\mathbf{R})$, the difference between the periodic Stokeslet and the regular Stokeslet, as defined in Eq. (29).

Since $\tilde{\mathbf{S}}_{\mathrm{p}}(\mathbf{R})$ is defined through sums, although rapidly converging, in real and Fourier space, it is more costly to evaluate than a Green's function with a closed analytical expression. Therefore, we initially evaluate $\tilde{\mathbf{S}}_{\mathrm{p}}(\mathbf{R})$ on a uniform grid with grid size h_{g}, covering the periodic box $[-\gamma_x/2,\gamma_x/2]\times[-\gamma_y/2,\gamma_y/2]\times[-\gamma_z/2,\gamma_z/2]$, later using trilinear interpolation to compute $\tilde{\mathbf{S}}_{\mathrm{p}}(\mathbf{R})$ for any $\mathbf{R}$. This works well since $\tilde{\mathbf{S}}_{\mathrm{p}}(\mathbf{R})$ is a smooth function.

In the evaluation of $\tilde{\mathbf{S}}_{\mathrm{p}}(\mathbf{R})$, the infinite sums in its definition must be truncated, but we must retain enough terms to guarantee sufficient accuracy. Let $Z(N)=\{i\in Z{:}-N\leqslant i\leqslant N\}$. We then define

$$\tilde{\mathbf{S}}_{\mathrm{p}}^{N_P,N_K}(\mathbf{R})=\tilde{\boldsymbol{\Upsilon}}(\mathbf{R})+\sum_{\substack{p_1,p_2,p_3\in Z(N_P)\\ |\mathbf{p}|\neq 0}}\boldsymbol{\Upsilon}(\mathbf{R}+\mathbf{p})+\frac{1}{\tau}\sum_{\substack{k_1,k_2,k_3\in Z(N_K)\\ |\mathbf{k}|\neq 0}}\hat{\boldsymbol{\Phi}}(\mathbf{k},\mathbf{R}). \tag{45}$$

In the computation of $\tilde{\mathbf{S}}_{\mathrm{p}}^{N_P,N_K}(\mathbf{R})$, $\xi>0$ is a free parameter to choose. As ξ gets larger, the real space sum will converge more rapidly and the sum in Fourier space more slowly; the opposite is true as ξ gets smaller. Hence, there is an optimal value of ξ. Pozrikidis [24] suggests $\xi=\sqrt{\pi}/\tau^{1/3}$, where $\tau=\gamma_x\gamma_y\gamma_z$ is the volume of the periodic box.

The sums converge the fastest for a square box with $\gamma_x=\gamma_y=\gamma_z$. In this case, we do find that $\xi=\sqrt{\pi}/\tau^{1/3}$ yields comparable truncation errors for the two sums when the same number of terms are included in real and reciprocal space, respectively. Consider $\gamma_x=\gamma_y=\gamma_z=2$, with grid size $h_{\mathrm{g}}=0.1$. Taking a maximum over all grid points, we find that $|\tilde{\mathbf{S}}_{\mathrm{p}}^{2,2}(\mathbf{R})-\tilde{\mathbf{S}}_{\mathrm{p}}^{8,8}(\mathbf{R})|$ is no larger than 2.3×10^{-7} for any of the matrix components. For $|\tilde{\mathbf{S}}_{\mathrm{p}}^{4,4}(\mathbf{R})-\tilde{\mathbf{S}}_{\mathrm{p}}^{8,8}(\mathbf{R})|$, the difference is smaller than round-off error (10^{-16}). Hence, a choice of $N_P=N_K=4$ offers sufficient accuracy.

For a box that is longer in one direction, like $\gamma_z>\gamma_x=\gamma_y$, the decay is not as excellent as is the case for the square box. With the choice of ξ above, the decay in physical and reciprocal space is no longer well balanced, with the decay in reciprocal space the slowest. To improve on this balance, we suggest a modified value of ξ,

$$\xi=\sqrt{\pi}/(\gamma_x\gamma_y\gamma_z\max(\gamma_x,\gamma_y,\gamma_z))^{1/4}. \tag{46}$$

This yields a more comparable decay in the two spaces, albeit still slower than in the optimal case of a square box. In the case of $\gamma_x=\gamma_y=\gamma_z=\gamma$ it reduces again to $\xi=\sqrt{\pi}/\tau^{1/3}=\sqrt{\pi}/\gamma$.

Define the periodic box $\gamma_x=\gamma_y=2$ and $\gamma_z=10$, and define ξ as in Eq. (46). With grid size $h_{\mathrm{g}}=0.2$, a maximum over all grid points yields that $|\tilde{\mathbf{S}}_{\mathrm{p}}^{4,4}(\mathbf{R})-\tilde{\mathbf{S}}_{\mathrm{p}}^{8,8}(\mathbf{R})|<1.5\times10^{-4}$ and $|\tilde{\mathbf{S}}_{\mathrm{p}}^{8,8}(\mathbf{R})-\tilde{\mathbf{S}}_{\mathrm{p}}^{16,16}(\mathbf{R})|<4.5\times10^{-16}$ for all matrix components. Hence, sufficient accuracy is achieved with $N_P=N_K=8$. It is clear that we need to include more terms in the sums compared to the square box. However, it is an improvement to change the definition of ξ. With $\xi=\sqrt{\pi}/\tau^{1/3}$, the comparable results are $|\tilde{\mathbf{S}}_{\mathrm{p}}^{4,4}(\mathbf{R})-\tilde{\mathbf{S}}_{\mathrm{p}}^{8,8}(\mathbf{R})|<2.4\times10^{-3}$ and $|\tilde{\mathbf{S}}_{\mathrm{p}}^{8,8}(\mathbf{R})-\tilde{\mathbf{S}}_{\mathrm{p}}^{16,16}(\mathbf{R})|<8.5\times10^{-12}$.

Hence, in this paper we will use ξ as defined in Eq. (46) with an equal number of terms in the sums in real and reciprocal space, with that specific number depending on the shape of the periodic box.

The tabulation of values of $\tilde{\mathbf{S}}_{\mathrm{p}}(\mathbf{R})$ needs only be done once in the beginning of the simulation. In fact, since the values of $\tilde{\mathbf{S}}_{\mathrm{p}}(\mathbf{R})$ depend only on the size of the periodic box, it can be tabulated once for a certain box size, then saved to file and simply read from file in the beginning of a new simulation.

Once $\tilde{\mathbf{S}}_{\mathrm{p}}(\mathbf{R})$ has been tabulated on a uniform grid with grid size h_{g}, we use trilinear interpolation to evaluate $\tilde{\mathbf{S}}_{\mathrm{p}}(\mathbf{R})$ for any $\mathbf{R}$. For this evaluation, all $\mathbf{R}$ vectors must be periodically modulated so that they fall into the periodic box. Since $\tilde{\mathbf{S}}_{\mathrm{p}}(\mathbf{R})$ is a smooth function, the trilinear interpolation is second order accurate, and the error is $\mathrm{O}(h_{\mathrm{g}}^2)$.

To solve for the coefficients in the force expansion, we need to evaluate $\tilde{\boldsymbol{\Theta}}_{\mathsf{lm}}^{kn}$ as given in Eq. (38). Here, we are integrating over $\mathbf{G}_{\mathbf{p}}^{\mathsf{lm}}(\cdot)$, as defined in Eq. (39). When $\mathsf{l}\neq\mathsf{m}$, $\mathbf{G}_{\mathrm{p}}^{\mathsf{lm}}(\mathbf{R})=\mathbf{G}(\mathbf{R})+\tilde{\mathbf{S}}_{\mathrm{p}}(\mathbf{R})$. Here, we can either add the two parts first, and then integrate, or first integrate separately, and then add the result. We will do the latter, applying analytical integration to $\mathbf{G}(\mathbf{R})$, as discussed in Section 4.2. For all other integration we use Gauss quadrature, also as discussed in the same section. The same approach is taken to evaluate the integrals over $\mathbf{G}_{\mathbf{p}}^{\mathsf{lm}}(\mathbf{R})$ for the evolution equations (40) and (41).

5. Convergence and accuracy

To validate the accuracy of our numerical method a number of test runs are performed to check the convergence with respect to the time step, Δt, the number of terms in the force expansion, N, and the number of quadrature intervals, N_q (analytic integration is used for inner integral as discussed in Section 4.2). In the periodic case we also examine how the accuracy is influenced by the step size, h_g, of the grid where the periodic Stokeslet contribution $\tilde{\mathbf{S}}_p$ (Eq. (29)) is tabulated.

All runs are performed with four fibers and the fibers are initially distributed randomly in a box defined by $x = [-2, 2]$, $y = [-2, 2]$ and $z = [-2, 2]$, see Fig. 1, where we also present the solution at the end time $t = 6$.

The order of convergence is determined by measuring the difference in fiber positions at the end time of consecutive solutions (obtained by variation of one of the parameters while the others are kept fixed). We define the difference in computed position as the maximum Euclidean distance between the two. That is, for one fiber with center positions and tangent vectors $\mathbf{x}_1$, $\mathbf{t}_1$, obtained with one set of parameters and for the same fiber but with $\tilde{\mathbf{x}}_1$, $\tilde{\mathbf{t}}_1$ obtained with a different set of parameters, we compute

$$\max_{s\in[-1,1]} \|\mathbf{x}_1 + s\mathbf{t}_1 - (\tilde{\mathbf{x}}_1 + s\tilde{\mathbf{t}}_1)\|,$$

where the norm is the Euclidean distance for a vector in $\mathbb{R}^3$.

The fiber position and orientation vectors are updated by applying the second order time stepping scheme in Eq. (43) to Eqs. (24) and (25) or Eqs. (40) and (41) in the periodic case. To check the convergence, five set of runs were made with $\Delta t = 0.3$, 0.15, 0.075, 0.03750 and 0.01875. The number of terms in the force expansion was $N = 5$ and the number of quadrature intervals was $N_q = 8$. In the periodic case the resolution of the grid on which $\tilde{\mathbf{S}}_p$ is tabulated was $h_g = 0.2$. The result is presented in Fig. 2. The convergence rate based on the consecutive solutions varies between 1.94 and 2.00 in the non-periodic case and 1.89 and 2.01 in the periodic case. In this case the error is of order 10^{-3} when $\Delta t = 0.1$ which is sufficiently accurate for our purposes.

Considering the fact that the total computational time is dependent on the size of Δt we would like to use as large time step as possible and in the absence of any strict stability restriction on Δt, the accuracy will be the limiting factor.

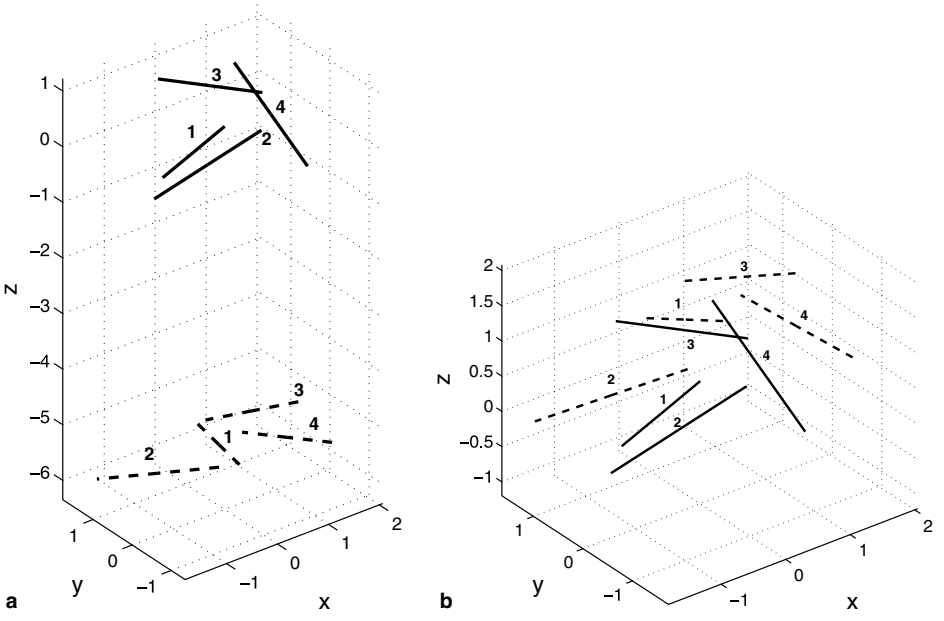

Fig. 1. Fiber configuration presented at $t = 0$ and $t = 6$ (dashed). In the periodic case the fibers has moved approximately one period in the z-direction. (a) Non-periodic case, (b) periodic case.

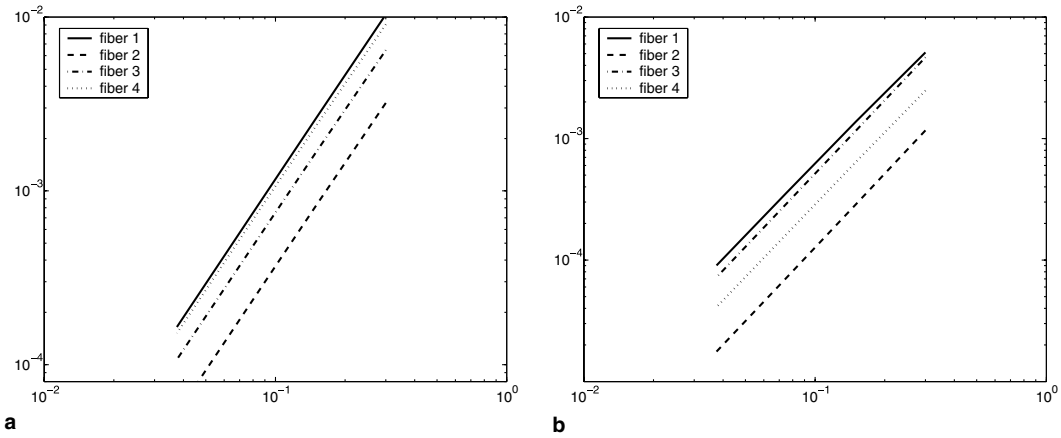

Fig. 2. The error in fiber position plotted as a function of Δt for the four different fibers at the end time $t = 6$. In both cases the convergence rate is close to second order. (a) Non-periodic case, (b) periodic case.

The force acting on a fiber is expanded in $N + 1$ Legendre polynomials and we want to investigate how the choice of N influences the error. Results are presented in Fig. 3(a) for solutions computed using $N = 1, 2, 4, 6, 8$. The other parameters were $\Delta t = 0.01875$ and $N_q = 8$.

As expected, we note that the errors decay as the number of terms in the force expansion increases, see Fig. 3(a). In the worst case, the difference between using $N = 8$ and $N = 6$ is of order 1.0×10^{-3} and between using $N = 6$ and $N = 4$ is of order 4.0×10^{-3}. In the numerical simulations presented in this paper we have used $N = 5$.

To compute $\mathbf{\Theta}_{lm}^{kn}$ (Eq. (23)), the inner integral is evaluated analytically using the formulas introduced in Section 4.2. By using analytical integration instead of numerical quadrature, it is possible to accurately handle the case when the distance between any two fibers is small. In this case $\mathbf{G}(\mathbf{R})$ in Eq. (23) becomes almost singular and a very large number of quadrature points would be needed to obtain an accurate solution if numerical quadrature were used.

The outer integral in Eq. (23) has to be evaluated numerically and the convergence rate with respect to the number of quadrature points is checked by performing runs with $N_q = 4, 8, 16, 32, 64$. The other parameters in the run were kept fixed at $\Delta t = 0.01875$ and $N = 5$. This was only done in the non-periodic case. In Fig. 3(a) we present the result for the four fibers. The average convergence rate over the different runs and the different fibers was 6.67 which is consistent with the formally sixth order accuracy of the three point Gauss quadrature rule.

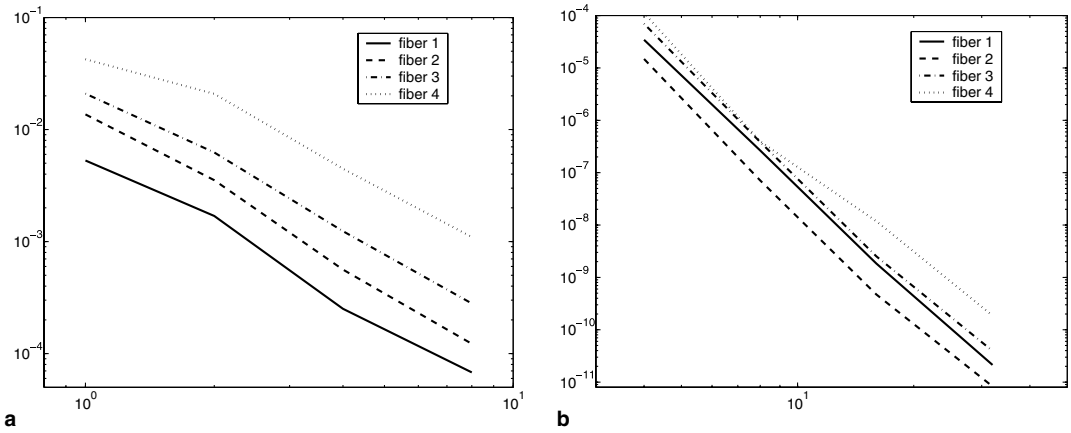

Fig. 3. The errors in fiber position for the four different fibers at the end time $t = 6$. $\Delta t = 0.01875$. In (a) error vs. N, $N_q = 8$, in (b) error vs. N_q, $N = 5$.

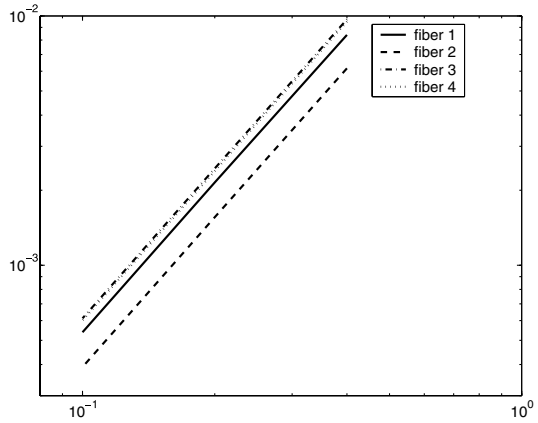

Fig. 4. The errors in fiber position vs. h_g for the four different fibers at the end time $t = 6$.

When we do periodic simulations, the periodic Stokeslet contribution $\tilde{\mathbf{S}}_p(\mathbf{R})$ (Eq. (29)) is initially evaluated on a uniform grid with a resolution given by the step size h_g. To compute $\tilde{\mathbf{S}}_p(\mathbf{R})$ for any $\mathbf{R}$, trilinear interpolation is used. In Fig. 4, we present the convergence rate obtained when using $h_g = 0.4$, 0.2, 0.1, and 0.05. The convergence rates varies between 1.97 and 1.99 which is close to the second order accuracy expected for trilinear interpolation.

The maximum difference in position using $h_g = 0.1$ and $h_g = 0.05$ is of order 5×10^{-4} and we will use $h_g = 0.1$ in the computations. However, the over all computational cost is not influenced by the size of h_g since once $\tilde{\mathbf{S}}_p$ has been tabulated on a grid, it is saved to file and can be used for later computations.

6. Numerical results

In this section, we present numerical simulations of a collection of 25, 50 and 100 fibers sedimenting due to gravity, and discuss a variety of results obtained.

In Fig. 5, we present the configuration of fibers at four different times for a simulation with 50 fibers in a periodic box of size $[-2,2]\times[-2,2]\times[-8,8]$. The gravity is acting in the negative z-direction.

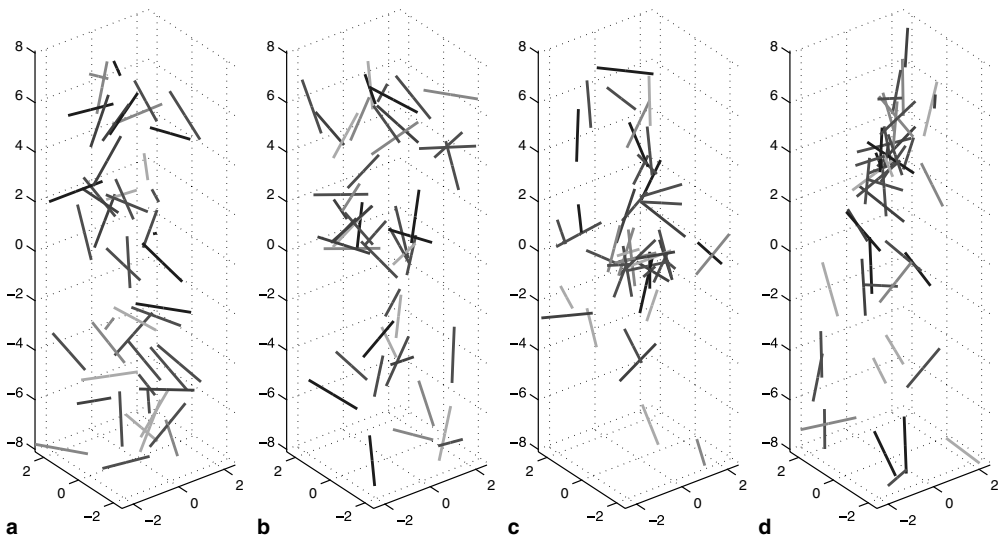

Fig. 5. Fiber configuration for 50 fibers with an initial random distribution shown at (a) $t = 0$, (b) $t = 30$, (c) $t = 60$ and (d) $t = 90$. The box size was $[-2,2]\times[-2,2]\times[-8,8]$.

The slenderness parameter used in the simulation was $\varepsilon = 0.01$. As usual, we use analytical integration for the inner integral in Eq. (23). For the outer integral, each fiber is divided into $N_q = 8$ subintervals and a three point Gauss quadrature rule is used on each interval. The time step was $\Delta t = 0.1$ and tabulation of $\tilde{\mathbf{S}}_p$, Eq. (29), is computed on a uniform grid with grid size $h_g = 0.1$. The solution has been computed until $t = 100$.

Initially, the fibers are randomly distributed. As time proceeds we can see how the fibers tend to align with gravity and forming clusters of fiber rich domains, slightly elongated in the z-direction, see Fig. 5. The experiments by Herzhaft and Guazzelli [14] verify the alignment of fibers in the vertical directions as well as large scale inhomogeneities in the fiber distribution during sedimentation. The fiber clustering was also observed in the experiments by Holm et al. [16].

We have also done a simulation of 100 fibers in the same periodic domain, and with the same numerical parameters. In this case the fiber concentration is larger but the behavior is similar to the run with 50 fibers, see Fig. 6. However, the alignment in the vertical direction is more pronounced and more than one cluster was formed.

In difference to spheres, isolated fibers can have motion perpendicular to gravity and the velocity depends strongly on the fiber orientation, [15]. Also, the forming of clusters, sometimes referred to as flocculation, is known to have an effect on the sedimentation velocity. Flocculation will enhance the settling velocity to a larger value than the maximum speed of a single and vertical aligned isolated fiber, the so-called Stokes velocity (equal to unity, with our non-dimensionalization). In the experiments by Herzaft and Guazzelli [14], they also found that the mean sedimentation velocity always reached a steady state value. In Fig. 7(a), we present the mean sedimentation velocity as a function of time for the two cases presented above with 50 and 100 fibers, respectively. The simulation box is of the same size for both cases, hence the concentration of fibers differs by a factor of two. In the case with 50 fibers, the mean sedimentation speed reaches a steady velocity around unity. In the case with 100 fibers the numerical simulations predict a larger settling velocity than unity and it has not reached a steady state value. The mean velocity in the horizontal direction is very close to zero, see Fig. 7(b).

In Fig. 8 the mean orientation of the fibers in the direction of gravity is shown as a function of time. We define the mean orientation as the average over all fibers of the absolute value of the z-component of the orientation vector, $\mathbf{t}$. It is clearly seen that after some time, the fibers tend to get aligned with the direction of gravity and a steady state mean orientation is obtained. The fibers are more aligned in the vertical direction for the case with higher concentration. This could explain why the mean sedimentation velocity is larger for this case.

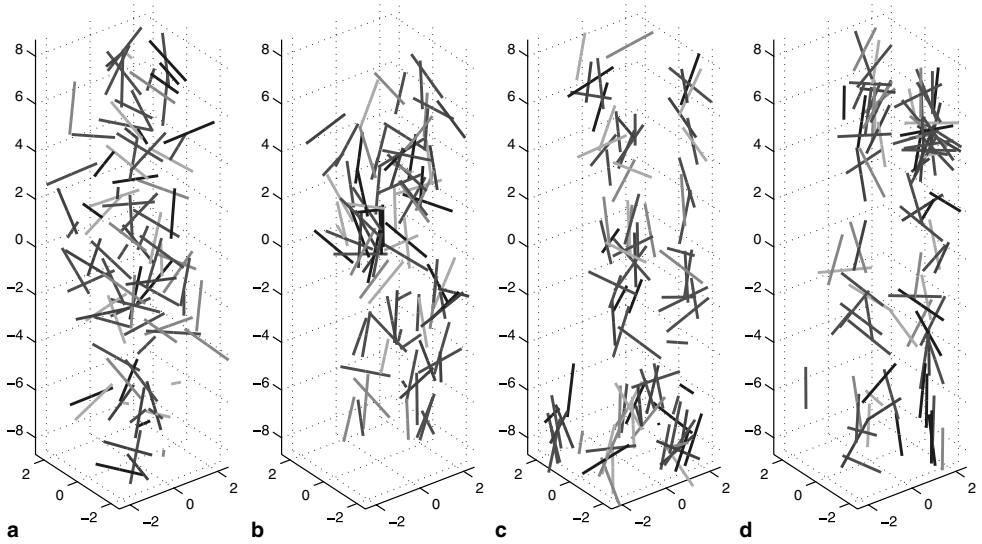

Fig. 6. Fiber configuration for 100 fibers with an initial random distribution shown at (a) $t = 0$, (b) $t = 30$, (c) $t = 60$ and (d) $t = 90$. The box size was $[-2,2]\times[-2,2]\times[-8,8]$.

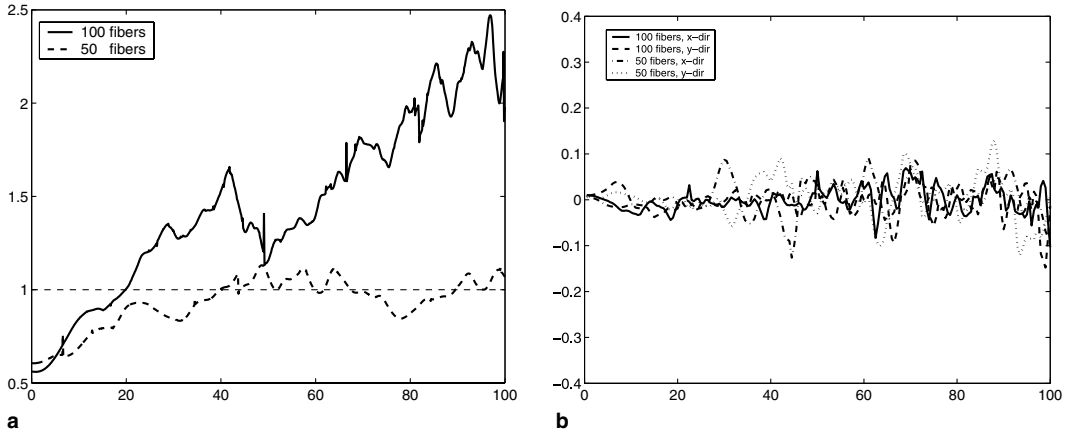

Fig. 7. Average velocity in (a) vertical and (b) horizontal directions as a function of time for different fiber concentrations. The vertical sedimentation velocity is defined as positive in the direction of gravity.

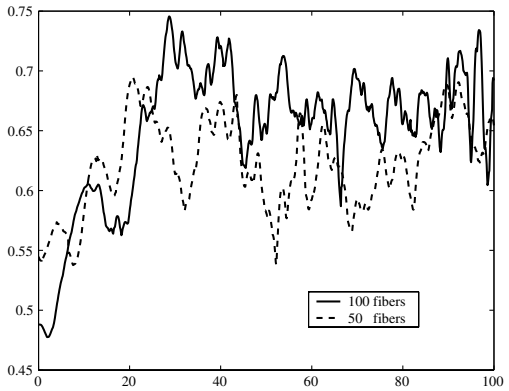

Fig. 8. Average orientation in the vertical direction for the simulations with 50 and 100 fibers.

Next we performed three runs where we kept the concentration of fibers constant. However, we used different numbers of fibers (25, 50 and 100) and in order to have a constant concentration the periodic box was scaled. The box dimensions in the horizontal direction were held constant and of size $[-2,2]\times[-2,2]$. The dimension in the vertical direction is given by $z\in[-2,2]$ for the case with 25 fibers. In the case of 50 fibers $z\in[-4,4]$ and finally in the case with 100 fibers, $z\in[-8,8]$. In Fig. 9, we present the average sedimentation speed and orientation for the three test cases. We see that both the average sedimentation speed and the mean orientation show similar characteristics for the three cases.

Finally, we also made two runs with 50 fibers using two different random initial configurations. In Fig. 10, we present the average sedimentation speed and the mean orientation obtained with the different initial configurations and the behavior is very similar. However, at the end of the simulation, the sedimentation speed in Fig. 10(a) is slightly higher (dashed line) in one case compared to the other. This could be explained by observing the dynamical process. After some time, a formation of cluster begins, and this clustering formation seems to reach a steady state where no more clusters are formed. Fibers are however leaving and entering the clusters. In the case with the higher sedimentation speed, only one large cluster was formed in the middle of the box. In the other case one cluster was formed close to one side of the box and a smaller cluster and a few isolated fibers were formed in the other end of the box.

As is mentioned in Section 3.4, we intend to later improve on our treatment of the interaction forces as the fibers come very close together. This will be important for simulations of densely packed suspensions. In the case of semi-dilute suspensions, studied here, theses short range forces should however have a rather limited

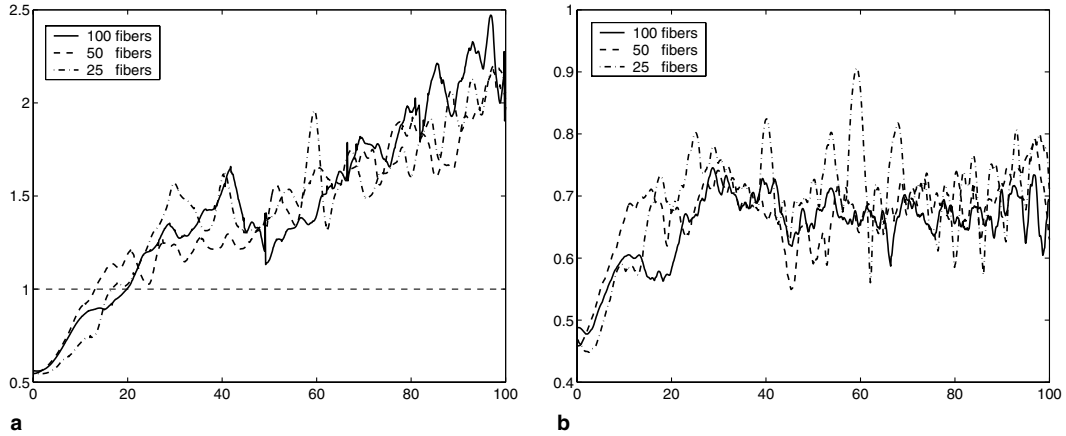

Fig. 9. (a) Mean sedimentation speed and (b) mean orientation for different number of fibers but at constant concentration. The size of the periodic box was kept constant in the horizontal directions and given by $x \in [-2,2]$ and $y \in [-2,2]$. In the vertical direction and 25 fibers: $z \in [-2,2]$, 50 fibers: $z \in [-4,4]$ and for 100 fibers: $z \in [-8,8]$.

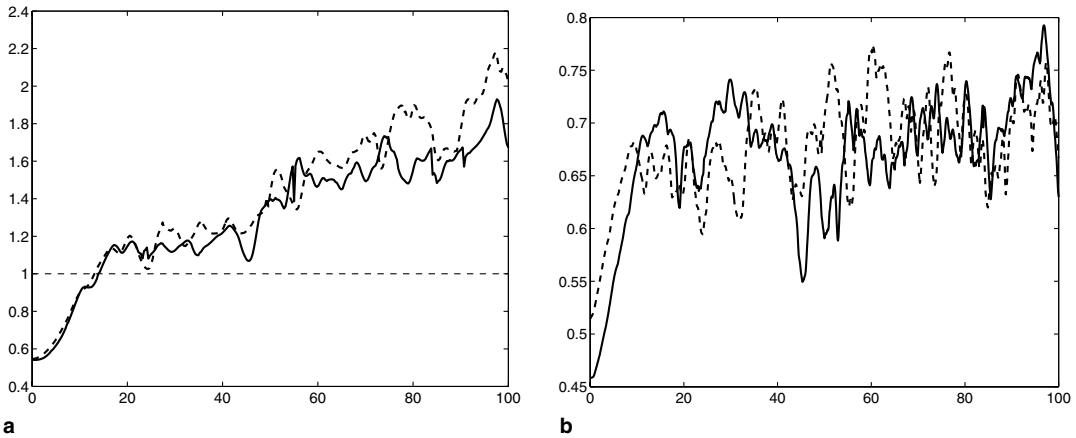

Fig. 10. (a) Mean sedimentation velocity and (b) mean orientation as a function of time for 50 fibers, but different initial configurations.

influence on the average behavior of the suspension. In [6], Butler and Shaqfeh compute the average sedimentation speed using a lubrication approximation and compare it to the sedimentation speed obtained without lubrication and the influence on the sedimentation speed was very moderate.

The aim with these simulations are to study a few characteristic features of the fiber suspensions such as average sedimentation speed and fiber orientation. However, to obtain quantities that are really representative, a larger number of fibers must be included in the simulations. There are also several other interesting features to study that requires the inclusion of more fibers, e.g., bulk properties such as the viscosity and permeability of the fiber suspension.

Currently, the computational cost prohibits including a larger number of fibers, and in order to enable larger simulations, a parallelization of the method will be done. Also as the number of fibers increase, the cost to compute the interactions between the fibers take up a majority of the computational time since it grows proportional to the square of the number of fibers. One possible way to reduce the cost of computing the fiber–fiber interactions is to use a modern fast summation algorithm like the fast multipole method. There are recent advances in the area of kernel-independent methods which can be applied to this problem, see Zorin et al. [4,27]. Another possibility would be to develop a pre-corrected FFT approach as described by Phillips and White [22]. Such methods can reduce the cost of the summation from $O(M^2)$ to $O(M \log M)$ or even $O(M)$, making this a key ingredient in a truly efficient numerical method.

7. Summary and conclusions

We have developed a numerical method for the simulation of rigid fiber suspensions, based on a non-local slender body formulation, that we have applied to simulations of the sedimentation of fibers due to gravity.

The slender body theory allows us to reduce a three-dimensional problem to a set of coupled one-dimensional integral equations along the fiber centerlines. The formulation is valid for Stokes flow, and contains the slenderness parameter ε, the radius to length ratio of the fiber. It is most accurate for the case of very slender fibers (small ε), the case that would be the most difficult to compute with a grid based method. Due to the computational cost that such a method would incur, to our knowledge, no such implementations are available.

The slender body equations are closed by imposing the constraints of rigid body motions. Manipulating the equations, and expanding the forces on Legendre polynomials to make use of the diagonalization result for the integral operator $\bar{\mathbf{K}}$, we obtain a linear system of equations for the coefficients in these expansions. The number of unknowns are $3NM$, where we have three coordinate directions, N terms in the force expansions (in addition to the constant term) and M fibers. With a typical value of $N = 5$, this means a total of 15 unknowns for each fiber. Once the force coefficients are known, the positions and orientations for the fibers can be updated by time-stepping separate ordinary differential equations.

In the periodic case, the Stokeslet included in the integrals defining the matrix entries for the linear system and the contributions to the translational and rotational velocities are replaced by the periodic Stokeslet. This periodic Stokeslet is decomposed into two parts. The first part is the regular Stokeslet, and hence contains the singularity as $|\mathbf{R}| \to 0$, where as the second part, that must be computed by evaluating one sum in real space and one sum in reciprocal space, is smooth. This latter contribution to the Stokeslet can hence be computed only once (the sums are both rapidly convergent) and be tabulated on a uniform grid, where a trilinear interpolation is used to compute the value at any desired point.

The inner integral over the Stokeslet and the dipole is evaluated by analytic integration, while the outer integral as well as integral over periodic contributions are computed using a three point Gauss quadrature (sixth order quadrature) on each of N_q subintervals. The time stepping scheme is of second order. We have presented convergence results and from those motivated our choices of the numerical parameters.

We have also performed larger simulations with up to 100 fibers sedimenting in a periodic box. Results from these simulations are used to study different properties of the suspension such as mean sedimentation speed and mean orientation of the fibers during the process. The simulations demonstrate that the suspension becomes anisotropic and that the fibers preferably align in the direction of gravity. Furthermore, the simulations also show that the fibers form clusters with an increase in sedimentation speed, above the maximum settling speed of an isolated fiber, as a result. This is in agreement with what has earlier been presented in both experimental work and numerical computations.

By now it is well known that the microstructure of the suspension has a large impact on its average behavior so it will also be of great interest to study how it influences other macroscopic properties such as effective viscosity and permeability. To perform extensive studies relating the microscale structure to theses various macroscopic properties, the efficiency of the code must however be enhanced, such that a larger number of fibers can be included in the simulations.

As was discussed in the previous section, the code will be parallelized and a fast summation method will be implemented to reduce what is now the dominating cost in any simulation with a relatively large number of fibers: the assembly (in each time step) of the linear system of equations for the force coefficients.

As we turn to suspensions of higher fiber concentrations, we will also return to a careful analysis of the close approach of two fibers, and the issue of how their interactions can be captured more accurately than our current slender body formulation allows for.

In our simulations all fibers have the same length. In many applications, there is however a variation in the length of different fibers. For spherical particles, effects of size distributions have been studied, but to our knowledge, there are no such studies in the case of fiber suspensions. Our formulation and implementation can be adopted to this interesting case in a straightforward manner.

While the fact that the fibers are straight has been explicitly used in the design of the numerical method to enhance its efficiency, the method can easily be applied to systems with other external forces and torques, as well as to problems with a non-zero background flow, such as a shear flow or an extensional flow.

Appendix A. Periodic Green's function for Stokes flow

The Stokeslet $\mathbf{S}(\mathbf{x})$ can be expressed as $\mathbf{S}(\mathbf{x}) = (\mathbf{I}\nabla^2 - \nabla\nabla)|\mathbf{x}|$. Following Pozrikidis [24], we decompose the Stokeslet, as written on this form, into two parts,

$$\mathbf{S}(\mathbf{x}) = \boldsymbol{\Upsilon}(\mathbf{x}) + \boldsymbol{\Phi}(\mathbf{x}),$$

where

$$\begin{pmatrix} \boldsymbol{\Upsilon} \\ \boldsymbol{\Phi} \end{pmatrix}(\mathbf{x}) = (\mathbf{I}\nabla^2 - \nabla\nabla)\begin{pmatrix} |\mathbf{x}|\mathrm{erfc}(\xi|\mathbf{x}|) \\ |\mathbf{x}|\mathrm{erf}(\xi|\mathbf{x}|) \end{pmatrix}, \tag{47}$$

where ξ is an arbitrary positive constant. This is a partition of unity, as the complimentary error function is defined as $\mathrm{erfc}(r) = 1 - \mathrm{erf}(r)$, with $\mathrm{erf}(r)$ as defined in Eq. (31). Hence, with $\xi = 0$, $\boldsymbol{\Phi}(\mathbf{x}) = \mathbf{0}$, and $\boldsymbol{\Upsilon}(\mathbf{x}) = (\mathbf{I}\nabla^2 - \nabla\nabla)|\mathbf{x}| = \mathbf{S}(\mathbf{x})$. As $\xi \to \infty$, the contribution from $\boldsymbol{\Upsilon}(\mathbf{x})$ vanishes and $\boldsymbol{\Phi}(\mathbf{x}) \to \mathbf{S}(\mathbf{x})$.

The idea now is to evaluate the periodic sum over $\mathbf{S}$ by evaluating the sum over $\boldsymbol{\Upsilon}$ in real space, and the sum over $\boldsymbol{\Phi}$ in Fourier space. We could of course use any function $f(\xi|\mathbf{x}|)$ and $1 - f(\xi|\mathbf{x}|)$ to decompose the Stokeslet, but it turns out that with a suitable choice of ξ, the choice of the error function yields a particularly fast decay, both for the sum in real space and the sum in Fourier space.

For $\boldsymbol{\Upsilon}(\mathbf{x})$, we can evaluate the expression in Eq. (47), to yield the result as defined in Eq. (33). For $\boldsymbol{\Phi}(\mathbf{x})$, we use Poisson's summation formula that states that for any function $F(\mathbf{x})$,

$$\sum_{p_1,p_2,p_3 \in Z} F(\mathbf{p}) = \frac{1}{\tau} \sum_{k_1,k_2,k_3 \in Z} \hat{F}(\mathbf{k}),$$

where $\hat{F}(\mathbf{k})$ is the three-dimensional Fourier transform of F. The vectors $\mathbf{p}$ and $\mathbf{k}$ are defined in Eqs. (27) and (35), respectively.

Using Poisson's summation formula, we rewrite the sum over $\boldsymbol{\Phi}(\mathbf{R} + \mathbf{p})$ as the sum in reciprocal space over $\hat{\boldsymbol{\Phi}}(\mathbf{k}, \mathbf{R})$, where

$$\hat{\boldsymbol{\Phi}}(\mathbf{k}, \mathbf{R}) = \int_{\mathbb{R}^3} \boldsymbol{\Phi}(\mathbf{R} + \mathbf{x}) e^{i\mathbf{k}\cdot\mathbf{x}} \, d\mathbf{x}. \tag{48}$$

The explicit form of $\hat{\boldsymbol{\Phi}}(\mathbf{k}, \mathbf{R})$, $\mathbf{k} \neq \mathbf{0}$, as given in Eq. (36) is derived by explicitly evaluating these Fourier coefficients, using the definition of $\boldsymbol{\Phi}(\mathbf{R} + \mathbf{x})$. See [24] for details.

This yields in total,

$$\mathbf{S}_{\mathrm{p}}(\mathbf{R}) = \sum_{p_1,p_2,p_3 \in Z} \boldsymbol{\Upsilon}(\mathbf{R} + \mathbf{p}) + \frac{1}{\tau} \sum_{\substack{k_1,k_2,k_3 \in Z \\ |\mathbf{k}| \neq 0}} \hat{\boldsymbol{\Phi}}(\mathbf{k}, \mathbf{R}). \tag{49}$$

Here, $\boldsymbol{\Upsilon}(\mathbf{x})$ decays rapidly (in a Gaussian manner) as $|\mathbf{x}| \to \infty$, and this sum is well defined. The coefficients $\hat{\boldsymbol{\Phi}}(\mathbf{k}, \mathbf{R})$, $|\mathbf{k}| \neq 0$ decay exponentially as $|\mathbf{k}| \to \infty$, and this is also a convergent sum. Omitted from this sum is the $|\mathbf{k}| = 0$ term.

A.1. Removing the divergent part

The periodic sum over the Stokeslet is divergent, yet the sum in Eq. (49) is convergent and hence well defined. We have reformulated the original sum by a partitioning into two parts, expressing the second part in Fourier space. The divergent part of the sum has been removed by omitting the $\mathbf{k} = \mathbf{0}$ term in Fourier space.

With $\mathbf{k} = \mathbf{0}$ in Eq. (48), we have

$$\hat{\boldsymbol{\Phi}}(\mathbf{0}, \mathbf{R}) = \int_{\mathbb{R}^3} \boldsymbol{\Phi}(\mathbf{R} + \mathbf{x}) \, d\mathbf{x}. \tag{50}$$

Since the integral is over all of $\mathbb{R}^3$, it will have the same value independent of $\mathbf{R}$, and we can let $\mathbf{R} = \mathbf{0}$ without loss of generality. We will perform the integration over a ball of radius R, eventually letting R tend to infinity. Let us express $\boldsymbol{\Phi}(\mathbf{x})$ in the form

$$\mathbf{\Phi}(\mathbf{x}) = S(\mathbf{x}) - \mathbf{\Upsilon}(\mathbf{x}) = \frac{1 - C(\xi|\mathbf{x}|)}{|\mathbf{x}|}\mathbf{I} + \frac{1 - D(\xi|\mathbf{x}|)}{|\mathbf{x}|^3}\mathbf{x}\mathbf{x}.$$

We introduce spherical coordinates, such that $r = |\mathbf{x}|$ and $\mathbf{x}\mathbf{x}/|\mathbf{x}|^3 = \hat{\mathbf{x}}\hat{\mathbf{x}}/|\mathbf{x}| = \hat{\mathbf{r}}\hat{\mathbf{r}}/r$, where the unit vector $\hat{\mathbf{r}} = \hat{\mathbf{r}}(\theta, \varphi)$, where $0 \leqslant \theta \leqslant \pi$ an $0 \leqslant \varphi \leqslant 2\pi$.

For the integration, we have that

$$\int_0^{2\pi}\int_0^{\pi} \sin\theta \hat{\mathbf{r}}(\theta,\varphi)\hat{\mathbf{r}}(\theta,\varphi)\,\mathrm{d}\theta\,\mathrm{d}\varphi = \frac{4}{3}\pi\mathbf{I},$$

such that

$$\begin{aligned}\int_{|\mathbf{x}|<R} \mathbf{\Phi}(\mathbf{x})\,\mathrm{d}\mathbf{x} &= \int_0^R\int_0^{2\pi}\int_0^{\pi} \mathbf{\Phi}(r\hat{\mathbf{r}})r^2\sin\theta\,\mathrm{d}\theta\,\mathrm{d}\varphi\,\mathrm{d}r \\ &= \left[4\pi\int_0^R \frac{1 - C(\xi r)}{r}r^2\,\mathrm{d}r + \frac{4}{3}\pi\int_0^R \frac{1 - D(\xi r)}{r}r^2\,\mathrm{d}r\right]\mathbf{I} \\ &= \left[\frac{8\pi}{3}R^2\mathrm{erf}(\xi R) + \frac{16\sqrt{\pi}}{3}R^3\xi\mathrm{e}^{-\xi^2R^2}\right]\mathbf{I},\end{aligned}$$

where we have used the definitions of C and D in Eq. (34). Using the definition of the error function, for $\xi > 0$ we have

$$\lim_{R\to\infty}\int_{|\mathbf{x}|<R} \mathbf{\Phi}(\mathbf{x})\,\mathrm{d}\mathbf{x} = \frac{8\pi}{3}R^2\mathbf{I}.$$

Hence, this is the divergent part of the sum (as multiplied by $1/\tau$), taken out by omitting the $\mathbf{k} = 0$ term from the reciprocal sum.

This limit is the same when the full sum is expressed in Fourier space, as in [13] (i.e., $\mathbf{\Phi}(\mathbf{x}) = \mathbf{S}(\mathbf{x})$), which is the case where $\xi \to \infty$.

The limit stays the same for this full range of ξ values since $\mathbf{\Upsilon}(\mathbf{x})$ decays rapidly in real space, and contains no long range contribution.

A.2. Better suited for computations

The periodic Stokeslet $\mathbf{S}_\mathrm{p}(\mathbf{R})$ can be efficiently computed numerically. With a suitable choice of ξ, both the sum in real space and in reciprocal space converge rapidly.

However, it does require more computational effort than to evaluate a regular Stokeslet. Hence, it is more efficient to initially compute the periodic Stokeslet on a uniform grid of points covering the periodic box, and then obtain the value at any given points by interpolation using these tabulated data.

As $|\mathbf{R}| \to 0$, the periodic Stokeslet does however have a $1/|\mathbf{R}|$ behavior, making it unsuitable to tabulate in a region where $|\mathbf{R}|$ is small. To obtain a function that is smooth, and hence can be tabulated for accurate interpolation on a regular grid, we decompose the periodic Stokeslet as $\mathbf{S}_\mathrm{p}(\mathbf{R}) = \mathbf{S}(\mathbf{R}) + \tilde{\mathbf{S}}_\mathrm{p}(\mathbf{R})$. With this decomposition, we have

$$\tilde{\mathbf{S}}_\mathrm{p}(\mathbf{R}) = \mathbf{S}_\mathrm{p}(\mathbf{R}) - \mathbf{S}(\mathbf{R}) = \mathbf{\Upsilon}(\mathbf{R}) - \mathbf{S}(\mathbf{R}) + \sum_{\substack{p_1,p_2,p_3\in Z\\ |\mathbf{p}|\neq 0}} \mathbf{\Upsilon}(\mathbf{R}+\mathbf{p}) + \frac{1}{\tau}\sum_{\substack{k_1,k_2,k_3\in Z\\ |\mathbf{k}|\neq 0}} \hat{\mathbf{\Phi}}(\mathbf{k},\mathbf{R}). \tag{51}$$

Let us now consider the first part, the two terms which both have a 1/—**R**— behavior. We have

$$\tilde{\mathbf{\Upsilon}}(\mathbf{x}) = \mathbf{\Upsilon}(\mathbf{x}) - \mathbf{S}(\mathbf{x}) = \frac{C(\xi|\mathbf{x}|) - 1}{|\mathbf{x}|}\mathbf{I} + \frac{D(\xi|\mathbf{x}|) - 1}{|\mathbf{x}|}\hat{\mathbf{x}}\hat{\mathbf{x}} = \frac{\tilde{C}(\xi|\mathbf{x}|)}{|\mathbf{x}|}\mathbf{I} + \frac{\tilde{D}(\xi|\mathbf{x}|)}{|\mathbf{x}|}\hat{\mathbf{x}}\hat{\mathbf{x}},$$

with $\tilde{C}(r) = C(r) - 1$ and $\tilde{D}(r) = D(r) - 1$, as defined in Eq. (30). This function is smooth as $|\mathbf{x}| \to 0$. To obtain the limits given in Eq. (32) as $|\mathbf{x}| \to 0$, we have used the limit

$$\lim_{|\mathbf{x}|\to 0} \frac{-\operatorname{erf}(\xi|\mathbf{x}|)}{|\mathbf{x}|} = -\frac{2\xi}{\sqrt{\pi}}.$$

Hence, $\tilde{\mathbf{S}}_{\mathrm{p}}(\mathbf{R})$ is a smooth function, and is suitable for tabulation. To obtain the full periodic Stokeslet $\mathbf{S}_{\mathrm{p}}(\mathbf{R})$, we simply add to $\tilde{\mathbf{S}}_{\mathbf{p}}(\mathbf{R})$ the Stokeslet contribution $\mathbf{S}(\mathbf{R})$, which can be directly evaluated for any $\mathbf{R}$.

Appendix B. Quadrature

The integrals

$$L_k^{\alpha,\beta} = \int_{-1}^{1} \frac{s^\alpha P_k(s)}{(\sqrt{s^2+bs+c})^\beta}\,\mathrm{d}s, \tag{52}$$

as given in Eq. (44) ($k = 0,\ldots,N$, $\alpha = 0,1,2$, and $\beta = 1,3,5$), can be evaluated analytically. The Legendre polynomial of degree k is given by

$$P_k(s) = \sum_{l=0}^{k} c_l s^l,$$

for some $c_l \in \mathbb{R}$, $l = 0,\ldots,k$. Hence, the highest power of s in the nominator in Eq. (52) will be of order $n = \alpha + k$ where $\alpha = 0,1,2$. So, in order to evaluate $L_k^{\alpha,\beta}$, for $k = 1,\ldots,N$, we need analytical expressions for the integrals

$$I_n^\beta = \int \frac{s^n}{(\sqrt{s^2+bs+c})^\beta}\,\mathrm{d}s, \quad n = 0,1,2,\ldots,N+2,$$

where $\beta = 1,3,5$.

To simplify the notation, introduce $u = \sqrt{s^2+bs+c}$ and $d = c - b^2/4$. For I_n^1 we have the recursive formula

$$I_n^1 = \frac{s^{n-1}u}{n} + \frac{(1-2n)b}{2n} I_{n-1}^1 - \frac{(n-1)c}{n} I_{n-2}^1 \quad n \geqslant 1,$$

where $I_0^1 = \ln|2s+b+2u|$. Note that for $n = 2$, the coefficient in front of I_{n-1}^1 vanishes.

For I_n^3 the recursion is

$$I_n^3 = I_{n-2}^1 - bI_{n-1}^3 - cI_{n-2}^3, \quad n \geqslant 2,$$

where

$$I_0^3 = \begin{cases} \frac{2s+b}{2du} & \text{if } d \neq 0, \\ -\frac{2}{(2s+b)^2} & \text{if } d = 0, \end{cases} \quad \text{and} \quad I_1^3 = -\frac{1}{u} - \frac{b}{2} I_0^3.$$

For I_n^5 we obtain

$$I_n^5 = I_{n-2}^3 - bI_{n-1}^5 - cI_{n-2}^5, \quad n \geqslant 2,$$

where

$$I_0^5 = \begin{cases} \frac{2s+b}{6du^3} + \frac{2}{3d} I_0^3 & \text{if } d \neq 0, \\ -\frac{4}{(2s+b)^4} & \text{if } d = 0, \end{cases} \quad \text{and} \quad I_1^5 = \begin{cases} -\frac{bs+2c}{6du^3} - \frac{b}{3d} I_0^3 & \text{if } d \neq 0, \\ -\frac{8}{3(2s+b)^3} - \frac{b}{2} I_0^5 & \text{if } d = 0. \end{cases}$$

B.1. Legendre polynomials

The Legendre polynomials are given by the following formula:

$$P_k(x) = 2^{-k} \sum_{n=0}^{[k/2]} (-1)^n \binom{k}{n} \binom{2k-2n}{k} x^{k-2n}, \quad k = 0,1,2,\ldots,$$

$$P_0(x) = 1,$$
$$P_1(x) = x,$$
$$P_2(x) = (3x^2 - 1)/2,$$
$$P_3(x) = (5x^3 - 3x)/2,$$
$$P_4(x) = (35x^4 - 30x^2 + 3)/8,$$
$$P_5(x) = (63x^5 - 70x^3 + 15x)/8,$$
$$P_6(x) = (231x^6 - 315x^4 + 105x^2 - 5)/16,$$
$$P_7(x) = (429x^7 - 693x^5 + 315x^3 - 35x)/16,$$
$$P_8(x) = (6435x^8 - 12012x^6 + 6930x^4 - 1260x^2 + 35)/128.$$

B.2. Gauss quadrature rule

The three point Gauss quadrature rule is given by

$$\int_{-1}^{1} f(x)\,\mathrm{d}x = \sum_{i=1}^{3} w_i f(q_i),$$

with the quadrature weights $w_1 = 5/9$, $w_2 = 8/9$, $w_3 = 5/9$ and quadrature points $q_1 = -\sqrt{15}/5$, $q_2 = 0$, $q_3 = \sqrt{15}/5$.

References

[1] G.K. Batchelor, Sedimentation in a dilute suspension of spheres, J. Fluid Mech. 52 (1972) 245–268.
[2] G.K. Batchelor, Slender-body theory for particles of arbitrary cross-section in Stokes flow, J. Fluid Mech. 44 (1970) 419–440.
[3] C.W.J. Beenakker, Ewald sums of the Rotne–Prager tensor, J. Chem. Phys 85 (1986) 1581–1582.
[4] G. Biros, L. Ying, D. Zorin, A fast solver for the Stokes equations with distributed forces in complex geometries, J. Comput. Phys. 193 (2004) 317–348.
[5] J.F. Brady, G. Bossis, Stokesian dynamics, Annu. Rev. Fluid Mech. 20 (1988) 111–157.
[6] J.E. Butler, E.S.G. Shaqfeh, Dynamic simulation of the inhomogeneous sedimentation of rigid fibers, J. Fluid Mech. 468 (2002) 205–237.
[7] I.L. Claeys, J.F. Brady, Lubrication singularities of the grand resistance tensor for two arbitrary particles, Phys. Chem. Hydrodyn. 11 (1989) 261–293.
[8] R.G. Cox, The motion of suspended particles almost in contact, Int. J. Multiphase Flow 1 (1974) 343–371.
[9] X. Fan, N. Phan-Thien, R. Zheng, A direct simulation of fibre suspensions, J. Non-Newtonian Fluid Mech. 74 (1998) 113–135.
[10] R. Glowinski, T.-W. Pan, T.I. Hesla, D.D. Joseph, A distributed lagrange multiplier/fictitious domain method for particulate flows, Int. J. Multiphase Flow 25 (1999) 755.
[11] T. Götz, Interactions of fibers and flow: asymptotics, theory and numerics, Ph.D. Thesis, University of Kaiserslautern, Germany, 2000.
[12] T. Götz, On collocation schemes for integral equations arising in slender-body approximations of flow past particles with circular cross-section, J. Eng. Math. 42 (2002) 203–221.
[13] H. Hasimoto, On the periodic fundamental solutions of the Stokes equations and their application to a viscous flow past a cubic array of spheres, J. Fluid Mech. 5 (1959) 317–328.
[14] B. Herzhaft, É. Guazzelli, Experimental study of the sedimentation of dilute and semi-dilute suspensions of fibres, J. Fluid Mech. 384 (1999) 133–158.
[15] B. Herzhaft, É. Guazzelli, M.B. Mackaplow, E.S.G. Shaqfeh, Experimental investigation of the sedimentation of a dilute fiber suspension, Phys. Rev. Lett. 77 (1996) 290–293.
[16] R. Holm, S. Storey, M. Martinez, D. Söderberg, Visualization of streaming-like structures during settling of dilute and semi-dilute rigid fibre suspensions, Phys. Fluid (accepted).
[17] R.E. Johnson, An improved slender-body theory for Stokes flow, J. Fluid Mech. 99 (1980) 411–431.
[18] J. Keller, S. Rubinow, Slender-body theory for slow viscous flow, J. Fluid Mech. 75 (1976) 705–714.
[19] E. Kuusela, K. Höfler, S. Schwarzer, Computation of particle settling speed and orientation distribution in suspensions of prolate spheriods, J. Eng. Math. 41 (2001) 221–235.
[20] A.J.C. Ladd, Hydrodynamic interactions in a suspension of spherical particles, J. Chem. Phys. 88 (1988) 5051–5063.
[21] B. Maury, Direct simulations of 2D fluid-particle flows in biperiodic domains, J. Comput. Phys 156 (1999) 325–351.

[22] J.R. Phillips, J.K. White, A precorrected-FFT method for electrostatic analysis of complicated 3-D structures, IEEE Trans. Comput. Aided Des. Integrated Circuits Syst. 16 (1997) 1059–1072.
[23] C. Pozrikidis, Boundary Integral and Singularity Methods for Linearized Viscous Flow, Cambridge University Press, Cambridge, 1992.
[24] C. Pozrikidis, Computation of periodic Green's functions of Stokes flow, J. Eng. Math. 30 (1996) 79–96.
[25] A.K. Tornberg, M.J. Shelley, Simulating the dynamics and interactions of flexible fibers in Stokes flow, J. Comput. Phys. 196 (2004) 8–40.
[26] Y. Yamane, Y. Kaneda, M. Dio, Numerical simulation of semi-dilute suspensions of rodlike particles in shear flow, J. Non-Newtonian Fluid Mech. 54 (1994) 405–421.
[27] L. Ying, G. Biros, D. Zorin, A kernel-independent adaptive fast multipole method in two and three dimensions, J. Comput. Phys. 196 (2004) 591–626.